

THE HOT INTERGALACTIC MEDIUM – GALAXY CONNECTION: TWO STRONG O VI ABSORBERS IN THE SIGHTLINE TOWARD PG 1211+143

JASON TUMLINSON¹, J. MICHAEL SHULL^{2,3}, MARK L. GIROUX⁴, & JOHN T. STOCKE²

Draft version September 17, 2018

ABSTRACT

We present *HST*/STIS and *FUSE* spectra of the QSO PG 1211+143 ($z_{em} = 0.081$) and a galaxy survey of the surrounding field. This sightline shows two strong intergalactic absorption systems at $cz \simeq 15,300$ and $19,300$ km s $^{-1}$. This sightline addresses the nature and origin of the O VI absorbers, and their connection to galaxies. We explore the relationship of these absorbers to the nearby galaxies and compare them to other O VI-bearing absorbers in diverse environments. At 15,300 km s $^{-1}$, we find four distinct H I components and associated C II, C III, C IV, Si II, Si III, Si IV, N V, and O VI, lying near a spiral-dominated galaxy group with a bright member galaxy $137h_{70}^{-1}$ kpc from the sightline. The observed ions of C, Si, and N are likely to be photoionized, but the O VI is more consistent with collisional ionization. The ion ratios in this absorber resemble the highly-ionized Galactic HVCs; it may also trace the hot intragroup medium gas or the unbound wind of an undiscovered dwarf galaxy. At 19,300 km s $^{-1}$, we find five H I components and associated C III, Si III, and collisionally-ionized O VI lying $146h_{70}^{-1}$ kpc from an isolated galaxy. The properties of the O VI-bearing gas are consistent with an origin in strong shocks between low-metallicity gas ($\geq 2 - 6$ % solar) and one or more of the warm photoionized components. It is likely that these absorbers are related to the nearby galaxies, perhaps by outflows or gas stripped from unseen satellite galaxies by interactions. However, we cannot reject completely the hypothesis that they reside in the same large-scale structure in which the galaxies are embedded but are otherwise not directly related.

Subject headings: intergalactic medium — quasars: absorption lines — quasars: individual (PG 1211+143)

1. INTRODUCTION

The uncertain role of hot (10^{5-7} K) gas in the intergalactic medium (IGM) and galaxy halos motivates us to seek out highly-ionized tracers in different environments. The most accessible tracer in this temperature range is the O VI $\lambda\lambda 1032, 1038$ doublet. With ionization energy of 114 eV required for its production, O VI arises in gas at $T = 10^{5-6}$ K in collisional ionization equilibrium (CIE; Sutherland & Dopita 1993). Two important scientific goals motivate the current observational searches for O VI absorption in the Galactic halo, Local Group, and IGM. First, O VI may help to locate some of the predicted “warm-hot intergalactic medium” (WHIM) thought to hold the 30 – 40% of baryons not yet accounted for at low redshift (Fukugita, Hogan, & Peebles 1998; Stocke, Shull, & Penton 2004b). Theory predicts that a substantial fraction of the baryons at low z are shock-heated to $T > 10^5$ K by gravitational infall into galaxies, groups, and other large-scale structures (Cen & Ostriker 1999; Davé et al. 1999). O VI could reveal the existence and location of some of these “missing baryons”. Second, the large *FUSE* survey of O VI (Sembach et al. 2003) suggests that hot gas forms an important component of the Milky Way halo and/or Local Group. Searches for O VI near other galaxies could generalize this result.

Hydrodynamical simulations (Cen & Ostriker 1999;

Davé et al. 1999) of large-scale structure predict that the low-redshift IGM is approximately equally divided by mass into three distinct phases: gas that has condensed to form stars and galaxies, gas that remains quiescently photoionized in the diffuse IGM ($T \sim 10^{4-5}$ K), and hotter gas ($T \sim 10^{5-7}$ K) that has fallen into the denser regions of the IGM where it is shock-heated and ionized. The cold, collapsed phase is well-understood from decades of studying galaxies. At low redshift, the photoionized phase has been studied extensively by *HST* (Bahcall et al. 1993; Penton, Shull, & Stocke 2000) and found to contain $29 \pm 4\%$ of the baryons in the local universe (Penton, Stocke, & Shull 2004, and references therein). The hot phase can be traced by the resonance lines of the highly-ionized species O VI, O VII, and O VIII. Tripp, Savage, & Jenkins (2000), Savage et al. (2002), and Danforth & Shull (2004) have found O VI absorbers in numbers that suggest that 5 – 10% of the baryons reside in the 10^{5-6} K phase, but X-ray searches for O VII and O VIII are just beginning with *Chandra* (Fang et al. 2002; Nicastro et al. 2002; Nicastro et al. 2004) and do not yet provide accurate baryon densities.

Another promising reservoir of hot gas lies in the extended halos of galaxies, as suggested by the discovery of widespread high-velocity O VI absorption in the environs of the Milky Way and/or Local Group by *FUSE* (Sembach et al. 2003). This survey found 84 distinct

¹Department of Astronomy and Astrophysics, University of Chicago, 5640 S. Ellis Ave., Chicago, IL 60637

²Department of Astrophysical and Planetary Sciences and CASA, University of Colorado, Boulder, CO 80309

³Also at JILA, University of Colorado and National Institute for Standards and Technology

⁴Department of Physics, Astronomy, and Geology, Box 70652, East Tennessee State University, Johnson City, TN 37614

high-velocity O VI systems in 102 surveyed extragalactic sightlines. While some of these highly-ionized clouds trace previously known H I structures, most do not, and their column densities and ionization conditions are too diverse to have a common origin. Instead, Sembach et al. (2003) and Collins et al. (2004) proposed a combination of photoionized and collisionally ionized models to explain the O VI. For the O VI without H I 21 cm emission, they favor a model in which O VI is collisionally ionized in interfaces between a hot ($\sim 10^7$ K), extended ($\gtrsim 70$ kpc, the distance to the Magellanic Stream) Galactic halo and cooler infalling material (Fox et al. 2004). In this model, the HVC O VI is an indirect indicator of the hotter gas rather than a major halo component in its own right. This key result also indicates that regions within 100 kpc of galaxies are fruitful places to search for the signatures of hot baryons participating in the formation and interaction of galaxies.

An alternative location for hot baryons is in the potential wells of galaxy groups, as proposed by Mulchaey et al. (1996). Intragroup gas in small, spiral-dominated groups is expected to have the right metallicity and temperature to show O VI as a direct signature of hot baryons. Although this prediction has yet to be confirmed, Shull, Tumlinson, & Giroux (2003) found O VI associated with a galaxy group on the sightline to PKS 2155-304. They suggested that this O VI is collisionally ionized in the interface between infalling cool gas and the hot intragroup medium, such that O VI serves as an indicator of the hotter WHIM gas, as it appears to in the Galactic halo.

Although the expected signatures of hot, shock-heated IGM gas have been identified in QSO absorption lines, their connection to galaxies is still largely unknown. Correlations between galaxies and Ly α clouds have been described in a statistical sense (Lanzetta et al. 1995; Chen et al. 2001; Bowen, Pettini, & Blades 2002; Penton, Shull, & Stocke 2000; Penton, Stocke, & Shull 2002, 2004). The locations of Ly α clouds (the warm phase) and the WHIM relative to galaxies can be examined at a phenomenological level with numerical simulations (Davé et al. 1999). However, observational evidence linking Ly α clouds and the WHIM to galaxies or large-scale structure is rare, owing to two technical barriers to large samples. First, obtaining high-resolution QSO spectra that cover all interesting IGM absorption lines is difficult. Second, these studies often must observe only the UV-brightest targets, which are usually selected without regard to the foreground galaxy populations. This factor entails intensive galaxy field surveys to follow up the spectroscopic studies. Both the high-quality spectra and complete galaxy redshift surveys are necessary to draw causal connections between IGM absorbers and galaxies. Once obtained, the data often yield inconclusive results on the origin of the absorbing material owing to line blending or insufficient column-density sensitivity. Thus, even though some IGM material shows evidence of influence from galaxies (generally metal enrichment), it is difficult to relate absorbers to individual galaxies or the large-scale structure in any general way. While most low column density Ly α absorbers are plausibly related to large-scale structure (Penton et al. 2002; Rosenberg et al. 2003), a compelling case for individual

cloud/galaxy associations can be made for only a few of the strongest Ly α absorbers (for example, 3C 273, Stocke et al. 2004a and PKS 2155-304, Shull, Tumlinson, & Giroux 2003).

In this study, we examine two strong, O VI-bearing IGM absorption-line systems toward PG 1211+143 and analyze their connections to galaxies. With $W_\lambda = 1130$ mÅ at $15,300$ km s $^{-1}$ and 880 mÅ at $19,300$ km s $^{-1}$, these systems are among the strongest Ly α absorbers at low redshift (Penton, Shull, & Stocke 2004). These systems address two major issues of recent concern to studies of the IGM. First, what is the nature and origin of the O VI absorbers? Second, what connection do these absorbers have to galaxies?

We describe our data and analysis techniques in § 2. In § 3 we discuss photoionization and collisional ionization models of the absorbers. In § 4 we compare these systems with other well-studied IGM and Galactic halo absorbers and discuss physical models for their origins. In § 5 we summarize our specific results on these absorbers and draw general conclusions about the connections between galaxies and the O VI-bearing IGM.

2. DATA AND ANALYSIS

2.1. STIS Data

The QSO PG 1211+143 ($V = 14.63$, $z_{em} = 0.081$) was observed for 67 ksec on 2002 February 4 – 8 with the *Hubble Space Telescope*/Space Telescope Imaging Spectrograph (E140M grating, $R = 44,000$; Program ID GO8571). The data were obtained from the STScI archive and calibrated by the standard CALSTIS calibration pipeline. The 16 sub-exposures were co-added with weighting proportional to their individual signal-to-noise ratios. The data span wavelengths from 1146 Å to 1726 Å in 44 echelle orders with a signal-to-noise ratio of 10 to 25 per 7 km s $^{-1}$ E140M resolution element.

The calibrated STIS spectra were examined for H I and metal absorption lines at the redshifts of the known Ly α complexes at $\simeq 15,300$ and $\simeq 19,300$ km s $^{-1}$, which were discovered with STIS G140M (Penton, Stocke, & Shull 2004). Figures 1 and 2 display continuum-normalized absorption-line profiles for the $15,300$ km s $^{-1}$ and $19,300$ km s $^{-1}$ systems, respectively, in heliocentric velocity space. In Figure 1 both lines of the O VI, C IV, and Si IV doublets are plotted. For the weaker lines in the C IV and Si IV doublets, the scale is drawn on the right axis and the data are shifted downward, such that the continuum line for the lower spectrum serves as the zeropoint of the upper spectrum. The component groups discussed in § 3 are marked with vertical dashed lines, and model absorption profiles are overlaid with solid curves. The component fitting and groupings are explained in § 2.3 and § 3.

2.2. FUSE Data

FUSE observed PG 1211+143 for 52.3 ksec on 2000 April 25 (observation P1072001). The *FUSE* satellite and its spectrograph performance are described by Moos et al. (2000), Sahnow et al. (2000), and in the *FUSE* Observer's Guide⁵. *FUSE* has an effective resolution that varies from $R = 15,000$ – $20,000$ over 910 – 1187 Å. We calibrated the data with CALFUSE 2.2.1, the latest version avail-

⁵Available online at <http://fuse.pha.jhu.edu/support/guide/guide.html>

able at the time of our analysis. The software applied a screen for detector bursts, extracted the one-dimensional spectrum from the two-dimensional detector images, and applied calibrations for wavelength and flux. We did not depart from the standard CALFUSE procedure, and we did not apply orbital day/night screening. We used all 37 sub-exposures in observation P1072001. The final effective exposure time was reduced to 51.7 ksec when detector bursts were excised. The *FUSE* SiC1 channel was not aligned with the other channels during the observation and provided no data. We applied small velocity shifts to the calibrated data to correct for the $\lesssim 10 \text{ km s}^{-1}$ systematic fluctuations in the *FUSE* wavelength solution. These corrections were derived by aligning interstellar Fe II and Si II lines detected in the STIS and *FUSE* data.

2.3. Line Fitting and Analysis

We analyzed the *HST*/STIS and *FUSE* absorption-line data with a combination of profile-fitting and direct-integration techniques. Absorption lines of interest were identified as lying within $\pm 500 \text{ km s}^{-1}$ of 15,300 and 19,300 km s^{-1} . The blended profiles were fitted as multiple components described individually by the column density N (cm^{-2}), heliocentric velocity $v \equiv cz$ (km s^{-1}), and doppler b parameter (km s^{-1}), together with a continuum composed of Legendre polynomials up to third order. The lines and continuum were fitted simultaneously by minimizing the χ^2 statistic and including Galactic interstellar molecular hydrogen (H_2) and atomic contamination where they exist; these contaminating lines are labeled in Figures 1 and 2. Individual velocity components in blended profiles were fitted simultaneously, but the Lyman series lines in each system were fitted separately to give relatively independent measures of the parameters. This provides a helpful check on uncertainties caused by blending, saturation, and the possibility of unseen components in the stronger lines. In most cases we adopt $N(\text{H I})$ from the profile fits from the higher Lyman lines (Ly β or Ly γ) because these are the only profiles where the components can be confidently separated. In some cases, certain parameters were fixed to help constrain the fit; these exceptions are noted below in § 3. The tabulated error bars correspond to 1σ confidence intervals on the parameters, obtained by finding the maximum and minimum parameter values giving $\Delta\chi^2 = 1$ from the best fit with all other parameters re-optimized. For both systems, the fitted H I columns were checked for consistency against a curve-of-growth analysis based on Ly α – Ly γ .

For *FUSE* data, we assume instrumental broadening by a Gaussian line spread function (LSF) with a full-width at half maximum (FWHM) corresponding to $R = 15,000$. For STIS data, we use the non-Gaussian LSF for the E140M grating and the $0.2'' \times 0.2''$ aperture ($R = 44,000$; see the STIS Instrument Handbook⁶). Formal doppler b parameters can be fitted down to the level at which the intrinsic FWHM ($\Delta v = 1.67b$) becomes comparable to the instrumental resolution. For STIS, we quote formally fitted linewidths down to $\simeq 5 \text{ km s}^{-1}$, but these narrow linewidths carry the additional uncertainty of being near the “effective” resolution including the broad wings of the STIS LSF. We can determine $b \gtrsim 12 \text{ km s}^{-1}$ from *FUSE*

data based on our assumption that $R = 15,000$ with a Gaussian line-spread function (*FUSE* can achieve up to $R = 20,000$ when subexposures are carefully aligned, but we assume $R = 15,000$ here to be conservative). However, there are some lines in the *FUSE* data that yielded formal best fits with smaller b , and other lines that were fitted with fixed $b < 12 \text{ km s}^{-1}$ based on linewidths for other species determined from the STIS data. These special cases are noted in the tables and in the discussion of these lines in the text. These linewidth uncertainties do not generally have adverse effects on the analysis.

The profile-fitting analysis generated the line parameters discussed in § 3. Consistent fit results across species are grouped according to velocity and are marked in Figures 1 and 2. These component groups are assumed to arise in the same gas and are interpreted as such in the sections below. See § 3 for details.

2.4. Galaxy Field

We compiled the available galaxy redshift data on the PG 1211+143 field to enable detailed comparisons between the IGM absorption-line systems and nearby galaxies (Table 1). The galaxy redshifts are drawn from the approximately 600,000 galaxies in the revised Center for Astrophysics redshift survey (Huchra et al. 1992; March 2004 version) and the several hundred galaxy redshifts near bright QSO sightlines obtained by McLin (2002; see also Stocke et al. 2005, in preparation). The combination of these galaxy catalogs provides a pencil-beam redshift survey that is complete to $m_B = 15.5$ for arbitrarily large impact parameter and to $m_B = 19$ for a $2.5'$ impact parameter to PG 1211+143. While the former magnitude limit, based on the CfA redshift survey, is a standard Zwicky blue-band magnitude, the deeper survey utilized red magnitudes corrected to m_B by assuming $B - R = 0.7$ (similar to an Scd galaxy). This conservative color assumption ensures that the quoted magnitude limit is appropriate for even quite blue galaxies. The Stocke et al. (2005, in preparation) magnitudes are 0.65 magnitudes brighter in the mean than measured blue magnitudes for a large sample of galaxies observed by several surveys. To be consistent, we have corrected the Stocke et al. (2005) magnitudes using the observed spectral energy distributions for the three galaxies that are not listed in the CfA catalog.

We do not believe that PG 1211+143 itself affects the quoted magnitude limit. At $cz = 19,300 \text{ km s}^{-1}$, an angular separation of $1''$ corresponds to $1.2 h_{70}^{-1} \text{ kpc}$ and our magnitude limit corresponds to a $\sim 0.3L^*$ galaxy. Therefore, we do not believe that we would have missed a galaxy at this limit or brighter because it was obscured by the QSO itself. At an impact parameter of $\lesssim 1''$, a much higher $N(\text{H I})$ absorber (i.e., a damped Ly α system) would be expected because the sightline would intercept the gaseous disk in this case (see e.g., Bowen, Tripp, & Jenkins 2001).

The galaxy field is pictured in Figure 3, and the galaxies lying within $|\Delta v| = 500 \text{ km s}^{-1}$ of the two absorber complexes are listed in Table 1. They range in projected separation from $\rho_{\perp} = 137h_{70}^{-1}$ to $889h_{70}^{-1} \text{ kpc}$ away from the QSO sightline (for Hubble constant $H_0 = 70h_{70} \text{ km s}^{-1} \text{ Mpc}^{-1}$). The seven CfA galaxies lie northwest of

⁶Available online at <http://www.stsci.edu/hst/stis/>

PG 1211+143 in a spiral-rich group $\sim 750h_{70}^{-1}$ kpc in projected extent with velocity dispersion $\sigma_{cz} = 150 \text{ km s}^{-1}$ (if the nearby galaxy at $cz = 14,888 \text{ km s}^{-1}$ is included, $\sigma_{cz} = 215 \text{ km s}^{-1}$). We have extended the Stocke et al. (2005) search for associated faint galaxies to the east and south of PG 1211+143 but have not discovered any additional galaxies at 15,300 or 19,300 km s^{-1} . Thus, the associated galaxies appear to be confined to the northwest of PG 1211+143. In § 4 we consider the possible connections between these galaxies, the group, and the absorbers in the PG 1211+143 sightline.

3. PHYSICAL CONDITIONS AND METALLICITY

In this section, we construct models for the PG 1211+143 absorption-line systems using a combination of photoionization equilibrium (PIE) and collisional ionization equilibrium (CIE) models. We break down the observed absorption profiles into individual velocity components, which are fitted separately but simultaneously. In some cases we allow these fits to be guided by expectations from modeling. We then regroup these components according to their common characteristics (e.g., ionization stage, linewidth, etc.) and analyze the groups as single systems. The grouped component systems are labeled in Tables 2 and 3 and include column-density limits on additional species when they constrain the models.

The proper interpretation of these complex absorption-line systems proceeds here in a three-step process. In the first step, we use the measured column densities, limits, linewidths, and relative velocities to diagnose the physical conditions indicated by the observed absorption. For our study, this means distinguishing PIE gas from CIE gas, and determining the physical conditions for each. The second step is the phenomenological step, in which we place these underlying physical processes in their proper context. For example, hot O VI-bearing gas can arise in shocks, turbulent mixing layers, or conductive interfaces – physically distinct origins that produce O VI with the same underlying physical process (ionization by thermal electron collisions). The third step in the interpretation is the selection of the phenomenological explanation that best fits the available information into a single physical picture. For example, we might argue that the O VI arises in material ejected from the nearby galaxies and shocked against photoionized Ly α forest gas in the galaxy's extended gaseous halo. The first two steps are carried out in this section. In § 4, we generalize the results derived here and discuss the possible causes of the O VI systems, including Galactic infall and outflow and hot-IGM models.

We model these absorbers with single-phase PIE and CIE models constructed using the CLOUDY code (version 94.00; Ferland et al. 1998). For PIE, we assume that the gas is optically thin to an extragalactic ionizing background with spectral shape from Shull et al. (1999). We normalize this extragalactic ionizing background to a specific intensity $J_\nu = 10^{-23} J_{-23} \text{ erg cm}^{-2} \text{ s}^{-1} \text{ Hz}^{-1} \text{ sr}^{-1}$ at 1 ryd. The measured value of J_{-23} is thought to be of order unity at $z \approx 0$ (Shull et al. 1999; Tumlinson et al. 1999). With a fixed radiation field, a variation in the photoionization parameter ($U \propto J_\nu/n_H$) represents a variation in the density n_H (cm^{-3}). Thus, for a given range in U , we state a corresponding range in density and line-of-sight extent for the gas, assuming $J_{-23} = 1$, with the caveat that

these quantities are directly and inversely proportional to the actual value of J_{-23} . We also vary the metallicity (Z) by scaling all heavy-element abundances relative to their solar values with a uniform scale factor. We then constrain the properties of the models to be compatible with all absorption-line measurements and limits associated with that velocity component. The quoted temperatures for model clouds are derived self-consistently within CLOUDY for each value of U and Z . For CIE, we use CLOUDY to calculate ion ratios as a function of temperature, ignoring radiation. We assume the updated solar abundances of carbon ($\text{C/H} = 2.45 \times 10^{-4}$; Allende Prieto et al. 2001a) and oxygen ($\text{O/H} = 4.90 \times 10^{-4}$; Allende Prieto et al. 2001b).

The conclusions we draw about the physical origins of these absorbers contain the implicit assumption that the gas is in either PIE or CIE. Because we consider only these mechanisms, the uncertainties in the physical state of the detected gas correspond only to the formal uncertainties in these models. There are other ionization mechanisms that may be able to produce the detected absorption, but which are much more difficult to constrain with the available information. One such mechanism is non-equilibrium collisional ionization (Shull & McKee 1979; Shapiro & Moore 1976), in which the gas possesses either enhanced high- or low-ionization states for its temperature. Such a model is difficult to constrain, and difficult to pursue for these absorbers. We cannot know whether the non-equilibrium gas was shocked to higher ionization, with a transient excess of low ions, or has recombined from a higher ionization state, with a transient excess of high ions. With such ambiguity we would not be able to connect the physical state of the gas to explanations for its origins, as we do for PIE and CIE in § 4. Also, the transient states associated with non-equilibrium collisional ionization are brief, so it is unlikely that all these absorbers would lie in such a state. We consider non-equilibrium ionization to be a possibility, but one which cannot be suitably tested against the data.

3.1. Physical Conditions in the 15,300 km s^{-1} System

The absorption-line system at 15,300 km s^{-1} shows a remarkably complex structure for a Ly α cloud. With profile fitting informed by reasonable inferences from photoionization models, we have identified eight distinct absorption components associated with the broad Ly α (1130 mÅ total equivalent width; Penton et al. 2004), six of which show metal-line absorption. These appear in Table 2 as A, B, B*, C, C*, and the O VI component (the asterisks denote that the component has the same velocity but higher ionization than its counterpart). Blending is severe in components B, B*, C, and C*, so we often fit more than one of them as a single component. Component D (15,407 km s^{-1}) appears in H I only; the apparent Si III $\lambda 1206$ in component D is a Ly α interloper at $cz = 13,035 \text{ km s}^{-1}$ that has been confirmed by a detection of Ly β in the *FUSE* data. The column density limits on metal lines do not provide a meaningful metallicity limit for this system. The weak component E (15,570 km s^{-1}) appears only in Ly α and has $N(\text{H I})$ too low for a meaningful metallicity limit to be determined. These Ly α -only components will not be discussed any further. We note that the Ly δ line at 15,300 km s^{-1} is blended with the Ly ϵ line from 19,300 km s^{-1} . Still higher Lyman series lines are too weak to give use-

ful information or are inaccessible due to blending, which is severe in the *FUSE* SiC2 channel below 1000 Å. The metallicity results for these components are summarized in Table 4.

A (15,288 km s⁻¹): This component shows H I, C III, and C IV. The H I at A is blended with the components B through C* in the Ly α and Ly β transitions, but in Ly γ it is possible to separate components A and B - C*. The H I and C III in this component present special difficulties in fitting. The fitted doppler b from C IV was used to fix the b for C III, which is poorly constrained on its own, owing to its location in the damping wing of Galactic Ly β . If the column density for H I is allowed to float, the best fit is obtained for $b_{HI} = 6$ km s⁻¹, which implies $T \leq 2200$ K, inconsistent with PIE models that produce C IV at $T \sim 30,000$ K and CIE models that produce C IV at $T \sim 10^5$ K. We therefore adopt column densities fitted with the assumption that $b_{HI} = 22$ km s⁻¹, or the thermal broadening corresponding to 30,000 K for H I (this is also the median value for Ly α absorbers; Davé & Tripp 2001). This assumption results in narrow error bars on the column density, and it has only a modest effect ($\lesssim 0.1$ dex) on the fitted column density of the H I associated with the B, B*, C, and C* components in Ly γ .

The 1σ ranges on the column densities of C III and C IV constrain a single-phase PIE model to have ionization parameter $-1.6 \leq \log U \leq -1.5$. With $\log N(\text{H I}) = 14.86 \pm 0.10$ set by Ly γ (the only profile where component A can be separately fitted), the metallicity of the gas is constrained to be $\log Z/Z_{\odot} \simeq -1.7 \pm 0.1$ (2% solar). The ionization parameter corresponds to a density $\log n_H \simeq -5.0 \pm 0.2$, pressure $P/k = 2.24n_H T \simeq 0.67$ cm⁻³ K, and line-of-sight extent $d = 180 - 400$ kpc. The corresponding range in temperature $T = 35,000 - 38,000$ K is marginally consistent with our assumption of $b_{HI} = 22$ km s⁻¹. We note that the small formal uncertainties in these parameters are due in large part to this assumption about the fitted b_{HI} . We use this component to illustrate the photoionization models we use throughout this section. Figure 4 shows the permitted $\pm 1\sigma$ ranges of C III and C IV column density, which overlap in the shaded region.

C IV (15,319 km s⁻¹): We also note the additional C IV component at 15,319 km s⁻¹, which does not appear to match any other metal-line or H I velocity component in the system, and therefore has not received its own label. If this C IV component arises in gas with $\log N(\text{H I}) \simeq 14.5$, $\log U \simeq -1.8$, and $Z/Z_{\odot} \simeq 0.1$, it is too weak to appear in any other species covered by our data. This PIE model predicts $\log N(\text{N V}) = 12.3$, $\log N(\text{C III}) = 12.7$, and $\log N(\text{O VI}) = 13.1$, below the levels that would be visible in the observed metal-line profiles. Because this ionization parameter and metallicity are roughly typical of the other components at 15,300 km s⁻¹, it is quite likely that this C IV component contributes little to the observed metal-line profiles. If we include an additional component with $\log N(\text{H I}) = 14.5$ and $b = 10 - 20$ km s⁻¹ in the fit to Ly γ , we find that it has minimal impact, within the 1σ errors, on every component but the highly uncertain component A. The quoted error for component A has therefore been increased from 0.05 to 0.10 dex to compensate. We have no other information about this component and cannot analyze it any further.

B and B* (15,340 km s⁻¹): This velocity component

appears in C III, Si III, C IV, and Si IV. Linewidths of $b \sim 20$ km s⁻¹ for both C III and Si III appear to distinguish the moderately-ionized component B from the highly ionized component B* seen in C IV and Si IV, which has $b \sim 7$ km s⁻¹. This disparity in linewidths is supported by the fact that it appears in data from both *FUSE* (C III) and STIS (Si III, Si IV, and C IV), with higher resolution. However, it may be that the saturated C III and strong Si III conceal additional weak, narrow components that align with the high ions. This possibility illustrates one reason why we cannot produce detailed photoionization models for these blended components. This issue is treated in more detail below during the discussion of all components B through C*.

C and C* (15,354 km s⁻¹): This velocity component appears in C II, Si II, Si III, C IV, and Si IV. These low- and high-ionization species have narrow linewidths and the same velocity, but we group them separately because they are not usually produced together in simple PIE models. For a grid of solar-metallicity models covering $-4 \leq \log U \leq -1$ and $\log N(\text{H I}) = 14.0 - 16.0$, we find that there is no single region of parameter space (U , N) that matches the observed column density of these five ions simultaneously. The ion pairs C IV-Si IV and C II-Si II appear together more commonly than the element pairs C II-C IV and Si II-Si IV. For this reason, we group the high ions and low ions together in different pairs. We define component C to include Si II and C II, and component C* to include C IV and Si IV. The narrow component in Si III at 15,356 km s⁻¹ could correspond to either one, but we place it with C*, consistent with most PIE models in which Si III goes with Si IV. A narrow component forced into the C III profile at this position does not substantially affect the fits for A and B in C III, but this additional C III component cannot be well-constrained in column density and linewidth. Since we do not attempt detailed models of these components, their exact groupings are not critical to our conclusions.

B, B*, C, C* combined (15,340 - 15,354 km s⁻¹): These four components and the 15,319 km s⁻¹ C IV component probably all contribute to the observed Ly α profile at 15,349 km s⁻¹ and the broad H I absorption in Ly β and Ly γ . Because these apparent components arise so closely together in velocity space, we now consider them all in relation to one another. Deriving detailed photoionization models for these blended and ambiguous components would require better knowledge of how to apportion the H I than we can derive from fits to the observed profiles. Because of this ambiguity, we have not attempted to match detailed photoionization models to the individual components. Instead, we seek three more modest goals: (1) to establish that photoionization is the likely production mechanism for the observed ion species; (2) to obtain reasonable estimates of or limits on the metallicity in one or more of the components; and (3) to determine the extent to which the observed O VI is associated with the gas traced by the low ions.

First, we assess the viability of CIE models for the moderately ionized gas seen in components B, B*, C, and C*. For B* and C*, we use the observed C IV/Si IV ratio to estimate $\log T \simeq 4.9 - 5.0$. In both B* and C*, the predicted and observed silicon linewidths are consistent ($b_{th}^{Si} \sim 7$ km s⁻¹), but the implied thermal linewidth for

carbon ($b_{th}^C \sim 11 - 12 \text{ km s}^{-1}$) is roughly twice the fitted value, and the implied $b_{th}^H = 40 \text{ km s}^{-1}$ thermal linewidth is too broad to fit the Ly γ profile⁷. We conclude that CIE is not viable for B* and C*. For component A, the one-to-one ratio of C III to C IV implies $\log T \simeq 5.0$, which predicts an H I linewidth $b_{th}^H \simeq 41 \text{ km s}^{-1}$, too broad for the observed Ly γ profile. For the narrow C component we derive $\log T \simeq 4.2$ from the C II/Si II ratio, but the implied H I column at this temperature is $\log N(\text{H I}) \simeq 16.5$, too high to be accommodated by the Lyman series profiles. In the case of the broad component B, CIE is viable at $\log T \simeq 4.8$, where $b_{th}^C \simeq 9 \text{ km s}^{-1}$ and $b_{th}^{Si} \simeq 6 \text{ km s}^{-1}$. These C and Si linewidths are consistent with the observed values if $b_{nt} \simeq 18 \text{ km s}^{-1}$, but the implied H I linewidth of $b_{th}^H \simeq 33 \text{ km s}^{-1}$ violates the observed linewidth constraint on H I ($b_{HI} = 6 - 22 \text{ km s}^{-1}$ fitted from Ly γ).

Since CIE has been eliminated as the source of ionization in the moderately ionized components B - C*, we next turn to photoionization models to judge their ability to produce the observed ionization. A grid of photoionization models ranging over $-4 \leq \log U \leq -1$ and $\log N(\text{H I}) = 14.0 - 16.0$ with solar metallicity shows that the observed column densities of C II-C IV, Si II-Si IV and their relative ratios can generally be produced for $\log N(\text{H I}) \simeq 14.5 - 15.0$, such that four components could be accommodated within the Ly γ profile. This means, however, that their metallicities, on average, cannot lie far below solar without violating the total H I constraint. This limit is especially severe for the Si II in component C, which requires $\log N(\text{H I}) \gtrsim 14.9$ at solar metallicity and higher $N(\text{H I})$ at sub-solar metallicity. This component must have $Z \gtrsim 40\%$ solar, even if we assign it all the available H I. Thus, at least one of the components with low-to-moderate ionization is expected to have a relatively high metallicity for diffuse IGM gas. In § 4 we interpret this as a clue to the absorbers' physical origins.

O VI (15,341 km s⁻¹): The strong O VI line provides a well-measured column density $\log N(\text{O VI}) = 14.26^{+0.05}_{-0.08}$. It is unclear how much H I is associated with this O VI. If it is photoionized, we can infer an acceptable range in metallicity and ionization parameter for an assumed $\log N(\text{H I})$ and judge whether the model is incompatible with the other absorption lines. Given the observed H I profiles, a column density of $\log N(\text{H I}) \simeq 14.5$ for photoionized O VI is assumed. Under this assumption we derive $-1.6 \leq \log U \leq -0.9$, $d = 46 - 2000 \text{ kpc}$, $-1.3 \leq \log Z/Z_{\odot} \leq 0$, and $T = 14,000 - 40,000 \text{ K}$. These models have $\log N(\text{C IV}) = 13.1 - 14.3$, $\log N(\text{C III}) = 12.5 - 14.1$, $\log N(\text{N V}) = 13.1 - 13.7$, and $\log N(\text{Si IV}) = 8.5 - 12.2$. At the lower end of these column density ranges, and with $b \simeq 53 \text{ km s}^{-1}$ for all species (dominated by the nonthermal broadening shown by O VI), these lines (especially C IV) are very difficult to exclude based on the observed profiles. However, such a model cannot readily explain the discrepancy between the predicted thermal linewidth for O VI ($b_{th}^O \leq 6.4 \text{ km s}^{-1}$ at $T \leq 40,000 \text{ K}$) and the observed value of $b_{OVI} = 53 \text{ km s}^{-1}$, which would need to be almost completely nonthermal. At the larger sizes, line broadening by the Hubble flow over 2 Mpc would exceed the observed linewidth. Although we consider this

model unlikely, owing to this linewidth discrepancy, we cannot exclude it on the basis of the predicted column densities alone. (See § 5 for a discussion of how photoionized and collisionally ionized O VI can be distinguished by X-ray observations.)

If the O VI is collisionally ionized, its linewidth corresponds to $2.8 \times 10^6 \text{ K}$ (with a 1σ upper limit of $T \leq 4 \times 10^6 \text{ K}$ at $b = 63 \text{ km s}^{-1}$), a temperature at which no other species covered by our data would appear (this model predicts $\log N(\text{H I}) \simeq 13.0$). At the maximum ionization fraction of O VI ($f_{OVI} = 0.22$ at $\log T \sim 5.45$), the predicted thermal linewidth for oxygen is $b_{th}^O = 17 \text{ km s}^{-1}$, requiring $b_{nt}^O = 50 \text{ km s}^{-1}$ to achieve the observed profile. An unconstrained portion of this additional linewidth may be velocity shear behind a bow shock. The contribution of shear lies in the range $\Delta V = (1 - 2)V_s \sin \theta \text{ km s}^{-1}$, where V_s is the shock velocity and θ is the angle between the infalling material and the shock vector. This shear contribution can be significant for shocks strong enough to generate O VI ($V_s \gtrsim 130 \text{ km s}^{-1}$), but θ is unconstrained. Given these uncertainties and the ambiguous apportionment of H I into the various photoionized components at the same velocity, we cannot derive the same robust temperature or metallicity limits for the O VI here as we do for the 19,300 km s⁻¹ system (see § 3.2). We consider collisional ionization to be a more likely mechanism than photoionization for the O VI, but the uncertainties in the nearby blended photoionized clouds preclude more definite conclusions.

3.2. Physical Conditions in the 19,300 km s⁻¹ System

This system consists of five components of H I (total Ly α profile equivalent width 880 mÅ; Penton et al. 2004) and moderate ionization species (C III and Si III) that appear to be photoionized (A, B, D). In addition, there are two strong O VI components with unclear alignment or association with the H I components. The E component appears in Ly α only and will not be discussed any further. We note that the Ly δ line at 19,300 km s⁻¹ is blended with the Ly δ line from 15,300 km s⁻¹. Still higher Lyman series lines are too weak to give useful information or inaccessible due to severe blending in the FUSE SiC2 channel below 1000 Å. The metallicity results for these components are summarized in Table 4.

A (19,274 km s⁻¹): This component is highly uncertain in both $N(\text{H I})$ and $N(\text{C III})$. The only distinct measurement of $N(\text{H I})$ comes from the A component of Ly γ , which exhibits a relatively narrow linewidth that is difficult to constrain. In the profile fits, we required that $b_{HI} \geq 10 \text{ km s}^{-1}$, which corresponds roughly to ionized gas at $T \gtrsim 8000 \text{ K}$. Below this temperature H will be only partially ionized and C III will not appear. This requirement leaves only a narrow range of permitted N and b for H I (see Table 3). The C III column density is also poorly constrained. However, we are still able to produce reasonable photoionization models. For the combined C III measurement and the C IV limit, we derive an ionization parameter range of $-2.8 \leq \log U \leq -2.5$. The corresponding range in temperature T is $8,700 \leq T \leq 16,300 \text{ K}$. We adopt $N(\text{H I}) = 14.46^{+0.12}_{-0.05}$ from the fit to Ly γ , which is

⁷For single-phase gas at temperature T , $b^2 = (2kT/m) + b_{nt}^2$, where m is the atomic mass and b_{nt} is the turbulent and/or non-thermal velocity dispersion.

less saturated and blended than Ly α and Ly β . The acceptable range in metallicity is $-0.4 \leq \log Z/Z_{\odot} \leq 0.0$. For $J_{-23} = 1$, the range in ionization parameter corresponds to a line-of-sight extent of 0.14 – 1.4 kpc. If we include the measured Si III and the limits on Si II and Si IV, the allowed parameter ranges narrow further to $-2.7 \leq \log U \leq -2.6$, $-0.2 \leq \log Z/Z_{\odot} \leq 0.0$, $-3.9 \leq \log n_H \leq -3.8$, $T = 9,500 - 12,900$ K and line-of-sight extent $d = 170 - 400$ pc. This absorber shows that additional species can constrain a photoionization model better than tighter limits on fewer species. Despite the large uncertainties in the profile fits, we believe that this component arises in warm, moderately photoionized gas with $\gtrsim 40\%$ solar metallicity⁸.

B (19,317 km s⁻¹): For the observed C III column density measurement and Si II and C IV limits, we find that this component is well-fitted by photoionization with $-3.0 \leq \log U \leq -2.4$. The corresponding range in temperature is $T = 13,000 - 23,000$ K. In this case, the constraints on the metallicity and the ionization parameter are highly correlated, but not narrowly constrained individually. For $\log N(\text{H I}) = 15.09^{+0.06}_{-0.07}$ (from Ly γ , the only profile where A and B can be separated), the acceptable range in metallicity is $-1.3 \leq \log Z/Z_{\odot} \leq -0.6$. For $J_{-23} = 1$, the range in ionization parameter corresponds to an extent of 0.23 – 7 kpc. This component appears to arise in warm photoionized gas but with less well-constrained properties than component A.

D (19,474 km s⁻¹): For the observed C III column density we find $-2.3 \leq \log U \leq -1.0$. The corresponding range in temperature T is $10,600 \leq T \leq 20,700$ K. For $\log N(\text{H I}) = 13.65$, from Ly β , the acceptable range in metallicity is $-0.2 \leq \log Z/Z_{\odot} \leq 0.0$. For $J_{-23} = 1$, the range in ionization parameter corresponds to an extent of 0.17 – 85 kpc. When combined with the upper limit $\log N(\text{C IV}) \leq 12.5$, this model yields ionization parameter $\log U \approx -2.2$, and metallicity $\log Z/Z_{\odot} \approx -0.1$, as well as an extent of ≈ 300 pc and a temperature $T \approx 11,000$ K. This component arises in warm, moderately photoionized gas with $\gtrsim 40\%$ solar metallicity. A model based on the lower $\log N(\text{H I}) = 13.40$ (within the errors on the Ly β fit) from the Ly α fit requires a correspondingly higher metallicity.

O VI (19,356 and 19,434 km s⁻¹): In addition to the three photoionized (C III- and Si III-bearing) components, this system exhibits two strong, broad O VI components. The O VI component at 19,356 km s⁻¹ lies well away from any clearly defined H I component, but the O VI line at 19,434 km s⁻¹ may correspond to Ly α component C. Here we discuss CIE models for both absorbers and PIE models for the second O VI.

First, we assume that the O VI line at 19,434 km s⁻¹ arises in the same single-phase photoionized gas as the Ly α component at 19,423 km s⁻¹ (C), as suggested by their close velocity coincidence and compatible linewidths. Under this assumption, we derive a range of ionization parameter $-0.9 \leq \log U \leq 0.0$, density $-6.5 \leq \log n_H \leq -5.6$, and temperature $T = 42,000 - 77,000$ K from the $N(\text{O VI})$ measurement and $N(\text{C IV})$ limit. With $N(\text{H I}) = 13.65$, this model gives metallicity $-1.7 \leq \log(Z/Z_{\odot}) \leq -1.3$ and line-of-sight extent $d = 400$ kpc to 44 Mpc. These larger

sizes are unreasonable, but there is a narrow range of parameter space with $d \sim 400$ kpc and $\sim 5\%$ solar metallicity that cannot be conclusively excluded. However, in this region, the model temperatures are $T \sim 40,000$ K, which is only marginally consistent with the observed H I and O VI linewidths. For $T = 42,000$ K and $b_{nt} = 10$ km s⁻¹, we derive $b_{HI} = 28$ km s⁻¹ and $b_{OVI} = 11$ km s⁻¹, much narrower than the observed b_{OVI} ; for larger cloud sizes the Hubble flow would broaden the line beyond the observed width. This last factor suggests that PIE is only a marginal fit to the available constraints. It is also rather unlikely that a region as large as 400 kpc would have been enriched uniformly to 5% solar metallicity. The O VI appears collisionally ionized, since $b_{th}^O = 17$ km s⁻¹ at $T = 10^{5.45}$ K, but we cannot completely reject PIE models for this O VI. As for the 15,300 km s⁻¹ system, the 19,434 km s⁻¹ O VI line could be photoionized if it is extremely large, metal-enriched, and substantially broadened by non-thermal motions.

However, the absence of associated C IV, clear-cut H I, and the broad linewidths of both O VI absorbers suggest that they are produced by CIE at $\log T \simeq 5.5$. We adopt this hypothesis and use the observed O VI column densities, the C IV limit, and the line profiles to constrain the temperature and metallicity of the ionized gas. For this purpose we use a conservative limit C IV, $\log N(\text{C IV}) < 13.1$, derived by integrating noise in the continuum over a 100 km s⁻¹ range for each O VI line (19,300 – 19,400 km s⁻¹ and 19,400 – 19,500 km s⁻¹). This limit corresponds to an unseen C IV line assumed to arise in the same gas as O VI, and therefore roughly as broad. For CIE and a solar C/O ratio, O VI achieves a higher column density than C IV at $\log T > 5.3$. The observed O VI columns and C IV limit (Table 3) combine to constrain the temperature to $\log T \geq 5.36$ for the $cz = 19,356$ km s⁻¹ absorber and to $\log T \geq 5.31$ for the $cz = 19,434$ km s⁻¹ absorber. These temperatures correspond to thermal linewidths of $b_{th}^O = 15$ km s⁻¹ for O VI and $b_{th}^H = 59 - 62$ km s⁻¹ for H I. The observed linewidths imply non-thermal broadening of $b_{nt} \leq 34$ km s⁻¹ and $b_{nt} \leq 15$ km s⁻¹ for the two components, respectively. Even if nonthermal broadening is ignored, these thermal linewidths are too broad to be consistent with the Lyman lines. This discrepancy suggests that if there is any significant H I associated with these collisionally ionized O VI lines, it is not carried by any of the identified components A – E.

With limits on the temperature and linewidths of the observed O VI, we can estimate the amount of associated H I present if we assume that the O VI arises at $\log T \simeq 5.45$, where it appears in CIE at its maximum ratio to H I, $\log [f_{OVI}/f_{HI}] = 5.13$. Off this peak, at higher and lower T , a given observed O VI column density will necessarily correspond to more H I. At this maximum value we can use the observed Ly α profiles to constrain the oxygen abundance O/H, where $\text{O/H} = \frac{N(OVI)}{N(HI)} \times \frac{f_{HI}}{f_{OVI}}$. We do this by adding to the profile fits two H I components at fixed cz and b corresponding to the observed O VI components. We allow $N(\text{H I})$ to vary to obtain a new best fit to the Ly α profile, and we obtain $\log N(\text{H I}) = 13.45$ at $cz = 19,356$ km s⁻¹ and $\log N(\text{H I}) = 13.44$ at $cz = 19,434$ km s⁻¹ (see bottom panel of Figure 2). For the solar O/H, these H I

⁸The integrated apparent column density measurement of $N(\text{C III})$, as described in § 4.5, restricts this model to $\log(Z/Z_{\odot}) \simeq -0.1$.

columns correspond to lower limits on the O abundance of $[O/H] \geq -1.19$ (6% solar) and $[O/H] \geq -1.63$ (2% solar), respectively. These are lower limits because we have maximized $\log[f_{OVI}/f_{HI}]$; off the peak at $\log T \simeq 5.45$, higher $[O/H]$ is necessary to match the observed O VI and still accommodate it within the Ly α profile. Thus, for CIE, we find that these hot clouds have $T \gtrsim 250,000$ K and $\gtrsim 2-6\%$ solar metallicity (see § 4.8 for an estimate of the IGM metallicity at ~ 150 kpc from galaxies.)

The broad linewidths of the detected O VI components suggest that they are collisionally ionized at $\log T \gtrsim 5.4$. We now explore the implications of this conclusion for the physical origins of this hot gas. In general, the production mechanism for hot, collisionally-ionized O VI in intergalactic space is not well understood. Known systems appear to arise from a diverse set of processes; among these are Galactic fountains, interfaces between hot substrates and infalling clouds, shear instabilities, and turbulent mixing layers. However, these processes have difficulty producing the observed column densities $\log N(O\,VI) \sim 14$ and ratios to C IV, Si IV, and N V (Indebetouw & Shull 2004a,b).

The most likely location for the collisionally ionized hot gas is the post-shock region behind a shock front between two interacting clouds (detectable O VI requires $\Delta v \gtrsim 150$ km s $^{-1}$ and $Z \gtrsim 0.01Z_{\odot}$). The physical conditions in the two O VI components and the presence of other IGM absorbers close in Δv motivate this view. The other detected species are consistent with a model in which the O VI is produced in the post-shock region of a cloud interacting with one of the warm photoionized components. To validate this model, we assume that a standard adiabatic shock achieves a post-shock temperature $T_s = (1.36 \times 10^5$ K) $(V_s/100$ km s $^{-1}$) 2 , where V_s is the shock velocity in km s $^{-1}$ and $\mu_s = 0.6m_H$ is the mean molecular weight of fully-ionized, post-shock gas with $n_{He}/n_H = 0.08$ (Shull & McKee 1979; Draine & McKee 1993). This relation and the temperature limits in CIE, set by $N(O\,VI)/N(C\,IV)$, determine which photoionized components (A - E) can trace the pre-shock material. Table 5 lists the relative velocities between the two O VI components and the photoionized components. In each case, three components have sufficient relative velocity to achieve the high post-shock temperatures ($\log T \gtrsim 5.3$) implied by the $N(O\,VI)/N(C\,IV)$ ratios. We also list the sound speed for the pre-shock gas as derived from the PIE models for components A, B, and D, and from the observed linewidth for E. These sound speeds and relative velocities imply strong shocks, with Mach numbers 7 - 19 and density enhancement approaching 4 behind the shock. The densities implied by the PIE models range from $\log n_H = -5.5$ to -3.2 . Together with the 2 - 6% solar metallicity limits derived for the O VI-bearing gas, these densities imply a radiative cooling time given by:

$$t_{\text{cool}} \lesssim (10^8 \text{ yr}) \left(\frac{10^{-4} \text{ cm}^{-3}}{n_H} \right) \left(\frac{0.03Z_{\odot}}{Z} \right). \quad (1)$$

If the O VI-bearing gas does not have substantially higher metallicity than the 2 - 6% lower limits implied by the line profiles, then the post-shock gas can have cooling times of > 1 Gyr at the lowest model densities ($\log n_H \sim -5.5$). At the higher densities and 30% metallicities, as in the photoionized components, the cooling time can approach 1

Myr, making it unlikely that absorbers of this type would be commonly seen. These lower densities for the post-shock gas imply pathlengths that are too long, favoring the higher densities permitted by the photoionization models.

The O VI-bearing components in the 19,300 km s $^{-1}$ system toward PG 1211+143 exhibit two robust features that favor their origin in collisionally ionized hot gas behind a strong shock front. First, they have linewidths too broad to be consistent with the H I and low ions seen nearby in velocity. Second, they have higher column densities than expected from some alternative models (conductive interfaces, turbulent mixing layers, Indebetouw & Shull 2004a). We favor a model in which the O VI arises behind strong shock fronts between low-metallicity clouds and one of the low-density photoionized components seen in H I and C III. This scenario is the simplest explanation for the observed column densities and line profiles that fits all of the available information. However, this picture does not uniquely constrain other important properties of the system. For instance, this picture does not depend on whether the O VI-bearing shocked material is ejected from or falling toward the nearby galaxy ($146h_{70}^{-1}$ kpc away at $|\Delta v| \sim 400$ km s $^{-1}$). In fact, this model does not require a causal connection between the galaxy and the absorbers. In § 4, we describe how such a connection could be established, and what it would mean for the IGM-galaxy connection.

4. PHYSICAL ORIGINS OF THE ABSORBERS

4.1. Physical Models of the Absorbers

In this section, we describe various physical models for the detected absorption complexes. These models complete the three-step interpretations begun in § 3 by placing the physical conditions, ionization mechanisms, and metallicities into the context of descriptive models. We consider galactic halo, high-velocity cloud, dwarf starburst wind, and intragroup medium models for the absorbers. We begin by comparing the PG 1211+143 systems with other O VI systems to see if trends emerge from the existing data.

Ongoing efforts to detect O VI in the low- z IGM with *FUSE* have found 127 Ly α absorbers ($W_{\lambda} \geq 80$ mÅ) with acceptable O VI data, 48 of which are detected in O VI at $\geq 4\sigma$ significance (Danforth & Shull 2004). Thus, $\sim 40\%$ of all Ly α absorbers contain both H I and O VI in the $N(H\,I)$ range for which high-quality *FUSE* spectra exist. The “multiphase ratio”, $N(H\,I)/N(O\,VI)$, varies substantially, from ~ 0.1 to greater than 100 (Danforth & Shull 2004), perhaps indicating a wide range in shock velocities and/or O/H abundances in these multiphase systems.

A smaller number of Ly α -O VI absorbers have been studied by both *FUSE* and STIS/E140M. We prefer these for detailed comparisons because they closely match the data quality, line coverage, and information content of the spectra we present here. Although the circumstances of the observations in these other studies are similar to our own, and we restrict our comparisons to only those systems that show O VI, their properties are quite diverse. Here, we make detailed comparisons to the STIS and *FUSE* studies of the sightlines H1821+643 (Tripp et al. 2001), PKS 2155-304 (Shull, Tumlinson, & Giroux 2003), PKS 0405-1219 (Chen & Prochaska 2000; Prochaska et al.

2004), 3C 273 (Sembach et al. 2001; Tripp et al. 2002), and PG 0953+415 (Savage et al. 2002).

4.2. Comparisons to 15,300 km s⁻¹

The system at 15,300 km s⁻¹ toward PG 1211+143 bears more than a superficial resemblance to the partial Lyman limit system (LLS) toward PKS 0405-1219 as reported by Chen & Prochaska (2000) and later studied thoroughly by Prochaska et al. (2004). Both systems show broad O VI offset in velocity from the strongest H I component, and both show clear multiphase structure with a wide range of ionization conditions. With $\log N(\text{H I}) = 16.45 \pm 0.05$, the PKS 0405-1219 system shows C II, C III, N II, Si II, Si III, Si IV, and N V at column densities 0.3 - 1.0 dex higher than we detect at 15,300 km s⁻¹ (the STIS data presented by Prochaska et al. 2004 did not cover C IV). This absorber has roughly 1 dex more H I than the PG 1211+143 15,300 km s⁻¹ absorber. This trend continues through the low ions (Si II, C II) and the moderate-to-high ions where they are available in both cases (Si III, Si IV). Accounting for higher N(H I), modest variations in ionization conditions, and radiative transfer effects (the Lyman limit system has $\tau_{LL} = N_{HI}/[1.59 \times 10^{17} \text{ cm}^{-2}] = 0.2$ at 1 ryd), it is possible that these complex, multiphase absorbers have a similar physical origin. For the low ions in the partial LLS, Prochaska et al. (2004) derive $\log U = -2.9 \pm 0.2$ and $\log Z/Z_{\odot} \gtrsim -0.3$, a metallicity similar to the range we infer for the low ions in the PG 1211+143 15,300 km s⁻¹ system. Their model for this cloud is a multi-phase partial LLS composed of photoionized gas in close association with a collisionally-ionized N V and O VI “skin” component offset from the main H I component.

In terms of their ionization states, column densities, linewidths, and component structures, the PG 1211+143 15,300 km s⁻¹ absorber and PKS 0405-1219 LLS are strikingly similar. They resemble one another in another critical aspect: both have bright galaxies at $\rho_{\perp} \sim 100h_{70}^{-1}$ kpc. PKS 0405-1219 has an elliptical galaxy at $75h_{70}^{-1}$ kpc with $|\Delta v| = 120$ km s⁻¹ and a spiral at $63h_{70}^{-1}$ kpc with $|\Delta v| = 30$ km s⁻¹. Although incomplete galaxy redshift information in the PKS 0405-1219 field hinders detailed conclusions, Chen & Prochaska (2000) conclude that both “Galactic halo” and “intragroup medium” models are viable locations for CIE and PIE gas to produce the observed column densities. This ambiguity also arises in the PG 1211+143 sightline. Improved galaxy/absorber statistics on sightlines passing near galaxies, within and outside groups, are necessary to determine the true physical origins of these intriguing absorbers.

4.3. Comparisons to 19,300 km s⁻¹

The 19,300 km s⁻¹ system toward PG 1211+143 shows strong C III, weak Si III, and two O VI components. While we cannot conclusively rule out photoionization models for the 19,434 km s⁻¹ O VI component if it is associated with the C component of H I, we favor an interpretation in which both O VI components arise in CIE hot gas at $\log T \gtrsim 5.45$, with the corresponding H I blended with the stronger photoionized systems. Regardless of the final interpretation, this system bears strong resemblance to the O VI systems at $z = 0.1212$ toward H1821+643 (Tripp et

al. 2001) and at $z = 0.00337$ toward 3C 273 (Sembach et al. 2001; Tripp et al. 2002). In all cases, broad O VI is seen, with some evidence of broad associated H I and an additional, narrower H I component that is not aligned with the O VI. The absence of metal-line absorption other than O VI in the H1821+643 and 3C 273 absorbers (down to the detection limits of their respective studies) may be a column-density effect; both systems have roughly one dex lower N(H I) than the PG 1211+143 19,300 km s⁻¹ system. If C III and Si III were present at the same metallicity and ionization parameter as in the other clouds, they would have gone undetected. The 3C 273 absorber is located $169h_{70}^{-1}$ kpc from a galaxy at $|\Delta v| = 90$ km s⁻¹, and the H1821+643 system is located $140h_{70}^{-1}$ kpc from a galaxy at $|\Delta v| \lesssim 30$ km s⁻¹.

The PG 1211+143 19,300 km s⁻¹ system also bears superficial resemblance to the $z = 0.14232$ system toward PG 0953+415 (Savage et al. 2002). This system shows H I, O VI, and (weak) C III. This system also lies in an apparent concentration of galaxies, with the closest being a bright galaxy at $|\Delta v| \sim 130$ km s⁻¹ and offset $\sim 400h_{70}^{-1}$ kpc from the sightline (the Savage et al. 2002 galaxy survey did not probe below $L \sim 0.5L^*$). However, this absorber shows O VI with a linewidth ($b = 13$ km s⁻¹) and column density ($\log N(\text{H I}) = 13.59$) that can be explained by a reasonable photoionization model with $\log(Z/Z_{\odot}) = -0.4$ and a 420 kpc line-of-sight pathlength. This system provides another interesting data point for correlations of O VI and metals with galaxies, but it does not parallel the PG 1211+143 systems as closely as do the others we compare to here.

The most striking feature common to all these absorbers is the velocity offset between the broad O VI components and the nearby strong, narrow H I. In 3C 273 the broad O VI lies in the wings of the photoionized H I profile. In PG 1211+143 the 19,356 km s⁻¹ O VI is not clearly aligned with any detected H I component, and any associated H I should also be broader than the detected H I. In H1821+143 and PG 1211+143, the velocity separations between the O VI and one or more of the H I components are consistent with an origin in post- and pre-shock gas in a strong shock front between the photoionized and O VI-bearing components, respectively. The small velocity separation in the 3C 273 cloud could be reconciled with this picture if the shock is viewed along its front and the shock velocity vector lies near the plane of the sky. Also, the absence of H I Ly α absorption at $z \approx 0.00337$ in the spectrum of RXJ 1230.8+0115 ($225h_{70}^{-1}$ kpc away) suggests a physical size to the O VI absorber smaller than plausible PIE models, thus favoring CIE for the 3C 273 absorber (Tripp et al. 2002).

Although there are some modest inconsistencies between these three cases, they together suggest that O VI can arise in collisionally ionized gas, shock-heated against lower ionization, photoionized gas which may or may not show metal-line absorption.

4.4. Extended Halos of Luminous Galaxies?

To address the question of whether these multi-phase, metal-enriched absorbers could be associated with the nearby galaxies, we review the evidence for causal associations between galaxies and Ly α forest clouds. In stud-

ies of Ly α absorption around galaxies, Chen et al. (2001) and Bowen, Pettini, & Blades (2002) concluded that tenuous [$\log N(\text{H I}) \gtrsim 13$] gas exists around galaxies out to $\rho_{\perp} \simeq 200h_{70}^{-1}$ kpc with a covering fraction near 100%. The PG 1211+143 systems lie within the scatter in the relations of Ly α equivalent width and/or $N(\text{H I})$ vs. impact parameter presented by these two studies. This consistency suggests that the PG 1211+143 systems may share a common physical origin with the Ly α absorption studied by these authors.

However, these previous studies differ in their physical interpretation. Chen et al. (2001) concluded that the strong correlation between $N(\text{H I})$ and ρ_{\perp} manifests a causal connection between the absorption and individual galaxies. They did not, however, evaluate the hypothesis that the H I traces not the individual nearby galaxies but rather the filamentary large-scale structure in which the galaxies are also embedded. Bowen et al. (2002) considered such a model and concluded that this latter hypothesis is just as likely as association with individual galaxies. They showed that the correlation between Ly α equivalent width and galaxy density at the redshift of their absorbers holds even if there is not a bright galaxy within $200h_{70}^{-1}$ kpc of the sightline. Similar statistical distributions of gas near galaxies have been reproduced in hydrodynamical simulations that minimize the active “feedback” from galaxies that would be expected to cause such a strong correlation (Davé et al. 1999). Similarly, using a larger (46 absorber) sample discovered with *HST* in regions surveyed for galaxies down to at least L^* , Penton, Stocke, & Shull (2002) found little statistical evidence that absorbers are associated with individual galaxies. With a few notable exceptions (e.g., the dwarf galaxy/absorber pair examined by Stocke et al. 2004a), a new study by Stocke et al. (2005, in preparation) obtains the same result, using a much larger absorber sample and extending the galaxy survey down to $0.1L^*$ luminosity. Similar results were obtained by Morris et al. (1993), Tripp, Lu & Savage (1998), and Impey, Petry & Flint (1999). These findings suggest that most low column-density absorbers are associated with large-scale galaxy filaments and not with individual galaxies. Thus, the current statistical evidence is, at best, ambiguous on the point of whether Ly α clouds, or a subset of the general Ly α forest population, are directly associated with nearby galaxies. However, the arguments for or against the association of Ly α clouds with galaxies cannot be automatically extended to the subset that are also O VI absorbers.

Unfortunately, the two absorbers toward PG 1211+143 only reinforce this ambiguity. The sightline clearly grazes the edge of a spiral-dominated group at $15,300 \text{ km s}^{-1}$ and passes within $150h_{70}^{-1}$ kpc of an apparently isolated galaxy at $19,300 \text{ km s}^{-1}$. These systems do, however, add one potentially critical piece of information to the puzzle – at least one component in each system shows near-solar metallicity. This metallicity is seldom if ever detected in the diffuse IGM, where $Z \sim 1 - 10\%$ solar is more typical. This factor suggests that these absorbers lie within the influence of the nearby galaxies, their smaller satellites, or the tidal streams created by their interactions. We explore

this hypothesis we explore in § 4.5.

Even if the observed H I is not associated with the extended halos of the nearby galaxies, the O VI might trace a hot, extended coronal halo with $T \gtrsim 10^6 \text{ K}$, as suggested for the Milky Way by a variety of studies (see Sembach 2003 for a review). For a hot, collisionally ionized corona of radius r , a sightline passing through its center will intercept a column density of O VI given by:

$$N(\text{O VI}) = 2(O/H)_{\odot} f_{\text{OVI}} r Z n_H \leq (2 \times 10^{12} \text{ cm}^{-2}) r_{150} Z_{0.1} n_{-5}, \quad (2)$$

where we have scaled to halo radius $r_{150} = r/150$ kpc, density $n_{-5} = n_H/10^{-5} \text{ cm}^{-3}$, and 0.1 solar metallicity, and adopted $f_{\text{OVI}} \leq 3.8 \times 10^{-3}$ at halo temperatures $T \geq 10^6 \text{ K}$. This simple model is therefore unable to reproduce the observed column density of $\log N(\text{O VI}) = 14.26$ at $15,341 \text{ km s}^{-1}$ at the temperature and density expected for a hot coronal galactic halo, even if the metallicity is solar. We also note that this simple model predicts $\log N(\text{H I}) \leq 12.3$, so this hot halo would not appear in either the Ly α halo studies quoted above or in our data. As O VII and O VIII are more abundant in CIE at these temperatures, such a scenario could be tested by X-ray observations of PG 1211+143 if sensitivity to $N(\text{O VII}) \simeq 10^{14} \text{ cm}^{-2}$ could be achieved.

Although the observed O VI does not provide direct evidence of a hot, galactic halo at $\sim 150h_{70}^{-1}$ kpc from these luminous galaxies, it may trace the interface between such a halo and cooler infalling material, as has been proposed for a subset of the local highly-ionized HVCs by Sembach et al. (2003) and Collins, Shull, & Giroux (2004). In this scenario, the O VI would serve as indirect evidence of the hot coronal halo. We turn to this issue in § 4.5.

4.5. *Extragalactic Analogs to High-Velocity Clouds?*

Since both PG 1211+143 cloud complexes contain O VI as well as other low- and high-ionization lines, it is useful to compare column density ratios found here with those found in O VI-bearing Galactic HVCs (Sembach et al. 2003) for which additional ions are available. These include the HVCs toward PKS 2155-304 and Mrk 509 (Collins et al. 2004), and PG 1259+593 (Fox et al. 2004). We list their high-ion column density ratios in Table 6, along with the measured values from the two PG 1211+143 systems.

For consistency with the HVC analyses, we depart from our method of fitting individual lines and instead integrate the apparent column densities of the metal-line absorption over velocity ranges set by the H I absorption. This apparent optical depth (AOD) method is valid for unsaturated lines (Savage & Sembach 1991) and appropriate for most of the fitted metal lines, so the high-ionization metal column-density ratios are not sensitive to this alternative method⁹. These column densities appear in Tables 2 and 3. While only limits exist on the high-ion ratios for the $19,300 \text{ km s}^{-1}$ systems, these limits suggest that this system is at least as highly ionized as the one at $15,300 \text{ km s}^{-1}$.

This comparison shows that the ratios in the $15,300 \text{ km s}^{-1}$ system would not be out of place in the dataset including the other O VI HVCs. The analyses of O VI

⁹This analysis gives model-independent measures of absorption in the overall line profiles which are generally consistent with the column densities derived from profile fitting in § 3.

HVCs by Collins et al. (2004) and Fox et al. (2004) favor models in which the O VI gas arises in conductive interfaces or turbulent mixing layers between photoionized gas and hotter gas (cf. Table 7 in Fox et al. 2004). The high-ion ratios in the 15,300 km s⁻¹ system lie near the region of parameter space occupied by shock ionization models and conductive interface models compiled by Fox et al. (2004) and Indebetouw & Shull (2004a), and assuming solar abundance ratios. The presence of lower ionization lines associated with the cooler gas makes these identifications plausible, as the cooler gas would be associated either with the pre-shock gas or the cooler side of the conductive interface. Fox et al. (2004) argue that the high ions associated with HVC Complex C arise in interfaces between the neutral HVC and a hot ($\sim 10^6$ K) Galactic halo. Models that associate the O VI gas with turbulent mixing layers predict a higher C IV/O VI ratio than the upper limits obtained here (assuming solar C/O). Considering the ratios alone, they seem more consistent with radiatively cooling gas flows, conductive interfaces, or shock ionization (as argued in § 3.2), indicative of more dynamically active environments such as dwarf galaxy outflows (see § 4.6).

However, an unequivocal explanation for the properties of the local O VI HVCs remains elusive. Based upon the present data, however, if such an explanation existed it could well be extended to explain the gas in the PG 1211+143 absorbers. A common explanation would rely on parallels between, for example, the PG 1211+143 systems and the low- N (H I) ionized skin of Complex C or the subset of Galactic O VI HVCs that do not show 21 cm emission (Sembach et al. 2003). These systems illustrate that, first, whatever mechanisms produce the Galactic highly-ionized HVCs, they can operate more than 100 kpc from a massive galaxy, and second, further searches near external galaxies should be undertaken to try to understand HVCs from the perspective of a projected, rather than radial, viewing geometry (e.g., Keeney et al. 2005). As the PG 1211+143 absorbers would appear as HVCs from the perspective of the nearby galaxies, they and systems like them could provide important clues to the origins of the local highly ionized HVCs.

4.6. Outflows from Nearby Galaxies?

The two bright galaxies known to be near the PG 1211+143 sightline suggest a model in which one or more of the absorption-line components arises in material flowing out of the nearby galaxies, perhaps in a starburst-driven superwind. Stocke et al. (2004b) review the literature on the potential connections between galaxies and Ly α absorbers. They outline a general picture in which most, and perhaps all, weak metal-line systems down to $N(\text{H I}) \simeq 10^{13-14}$ cm⁻² could arise in unbound winds from dwarf galaxies like the one they found near 3C 273. In this picture galaxies with $L \gtrsim 0.1L^*$ are too massive for starburst-driven winds to achieve escape velocity. This section considers the PG 1211+143 absorbers in the context of this picture.

Two of the best examples of nearby, weak metal-line systems are found in the sightlines to 3C 273 and RXJ 1230.8+0115, which are separated by 0.91°, or $363h_{70}^{-1}$ kpc at $cz = 1600$ km s⁻¹. Both sightlines have strong Ly α absorbers with $N(\text{H I}) \approx 10^{16}$ cm⁻² at similar

redshifts ($cz = 1586$ and 1666 km s⁻¹, respectively) and metallicities (6% and 10% solar; Tripp et al. 2002; Rosenberg et al. 2003). The 3C 273 absorber best illustrates the galactic superwind model. Stocke et al. (2004a) discovered a dwarf ($M_B = -13.9$, or $L = 0.004L^*$), post-starburst galaxy $70h_{70}^{-1}$ kpc away from the 1586 km s⁻¹ absorber. This galaxy/absorber connection is among the strongest in the literature: the absorber and galaxy redshifts match to within their combined errors, the absorbers and galaxy metallicities match to within their larger errors, and the absorber has an overabundance of silicon to carbon indicative of recent Type II supernova enrichment. The galaxy is a pure disk system showing both strong Balmer and metal absorption lines in its optical spectrum, and no evidence for dust or gas (no emission lines and $M_{\text{HI}} \leq 5 \times 10^6 M_{\odot}$; van Gorkom et al. 1993). From ratios of Lick absorption-line indices, Stocke et al. (2004a) estimate that the mean stellar age in this galaxy is 3.5 ± 1.5 Gyr.

Taken together, this information provides a consistent picture in which a massive ($\geq 0.3 M_{\odot}$ yr⁻¹) starburst ~ 3 Gyr ago created enough supernovae to blow the galaxy's remaining gas into the IGM. Because the dwarf is quite low in mass, this wind can easily escape from the galaxy and move to $\sim 100h_{70}^{-1}$ kpc at the 20 - 30 km s⁻¹ required to create the metal-line absorber seen toward 3C 273. This dwarf is estimated to have been ~ 10 times brighter when starbursting. However, no dwarf galaxy with similar properties or at comparable impact parameter has been found near the RXJ 1230.8+0115 absorber at 1666 km s⁻¹. Thus, even though the 3C 273 absorber establishes some of the necessary conditions for a successful dwarf superwind model, there is not yet sufficient evidence that this model is viable for all weak metal-line absorbers, although a galaxy survey near RXJ 1230.8+0115 at a depth comparable to the survey near 3C 273 has not been completed.

The dwarf galaxy superwind model does solve a difficult geometrical problem emphasized by Rigby et al. (2002): the small (10 pc - 10 kpc) sizes inferred for weak metal-line (Mg II, Fe II) absorbers are seemingly inconsistent with their high frequency in QSO spectra ($dN/dz \approx 1-2$ per unit redshift). A local example of this quandary is the three metal-line absorbers at comparable redshift in the 3C 273 and RXJ 1230.8+0115 sightlines. In this case, a single gaseous filament is probed by two random sightlines $\sim 363h_{70}^{-1}$ kpc apart, requiring high covering factor for metal-enriched ($Z \sim 2 - 10\%$ Solar) gas along this filament. This is easily explained by the dwarf superwind model because, while an individual superwind shell can be quite thin along any sightline, the spherical expanding shell subtends $\sim 100h_{70}^{-1}$ kpc on the sky. Thus, only 3-5 dwarf superwind outflows would be required to completely cover the area of this filament in metal-enriched gas. Because these dwarfs are typically fainter than $0.1L^*$, there would be little statistical evidence for absorber-galaxy associations in L^* galaxy samples (Bowen, Pettini, & Blades 2002) but rather strong evidence for absorber-galaxy filament associations, as has been found (Penton, Stocke & Shull 2002). This model also naturally reconciles the very small line-of-sight sizes inferred from PIE models for the metal-line absorbers in the 3C 273, RXJ 1230.8+0115, and PG 1211+143 sightlines with the large covering factors required to make this type of absorber relatively common

(see Stocke et al. 2004a; Rosenberg et al. 2003).

On the other hand, there is some evidence that more massive galaxies ($L \gtrsim 0.1L^*$) retain their metal-enriched gas in gravitationally-bound, optically-thick gaseous halos. Steidel (1995; 1998) found that almost all (53 of 55) strong Mg II absorbers, which are invariably optically-thick at the Lyman limit, have nearby, bright ($L \gtrsim 0.1L^*$) galaxies within $\sim 50h_{70}^{-1}$ kpc on the sky. In addition, in a recent study of the absorption lines associated with a luminous star-forming galaxy ($0.5L^*$, $SFR \simeq 1.4 M_\odot \text{ yr}^{-1}$) galaxy NGC 3067, Keeney et al. (2005) show that the strongest absorber [$N(\text{H I}) = 10^{20.0} \text{ cm}^{-2}$] in the spectrum of the quasar 3C 232 is not only gravitationally bound to the galaxy but is most likely infalling. Taking these various results into account, we would expect that the more luminous galaxies in the region of any QSO sightline would retain their gas in $\sim 50h_{70}^{-1}$ kpc bound halos.

When we consider the PG 1211+143 absorbers in the context of this picture, the conclusions are not as clear. First, of the three critical factors that enter the Stocke et al. (2004a) analysis, only the proximity (in impact parameter and velocity) and metallicity are available as discriminants for the PG 1211+143 absorbers. At least one of the components in each system has $Z \simeq 0.5 - 1.0 Z_\odot$, and both lie within $150h_{70}^{-1}$ kpc of bright galaxies. Lick indices measured from medium-resolution Las Campanas spectra (McLin 2002) indicate that neither galaxy has undergone a starburst in the last 3 Gyr. Both galaxies show old (3 - 8 Gyr), near solar-metallicity stellar populations, with modest ongoing star formation ($0.5 - 1.0 M_\odot \text{ yr}^{-1}$) in the galaxy at $15,242 \text{ km s}^{-1}$. This low level of star formation in a galaxy of $L \sim L^*$ is unlikely to have driven an unbound wind to $\sim 150h_{70}^{-1}$ kpc. We also have no evidence for elevated Si/C ratios that would indicate recent Type II SN enrichment¹⁰: the Si/C ratio at $15,300 \text{ km s}^{-1}$ is poorly constrained, and $[\text{Si/C}] \simeq -0.5$ at $19,300 \text{ km s}^{-1}$. The two galaxies nearest to the complex of PG 1211+143 absorbers are nearly L^* galaxies ($0.7 - 0.8L^*$ for $M_B^* = -19.6$ for $H_0 = 70 \text{ km s}^{-1} \text{ Mpc}^{-1}$; Marzke et al. 1994), and so would be expected to have bound halos by this model. Since their impact parameters to PG 1211+143 are twice as large as their expected halos, it is unlikely that outflows from these galaxies are directly responsible for the absorptions we see.

However, the 3C 273 case is relevant to the current cases if weak metal-line absorbers arise in starburst winds from dwarf galaxies fainter than our survey limit in this region ($m_B = 19$ out to 150 or $200h_{70}^{-1}$ kpc for these two absorbers, respectively). If placed at $15,000 - 19,000 \text{ km s}^{-1}$ the dwarf near 3C 273 would have $m_B \sim 22 - 23$, or $\sim 19.5 - 20.5$ while “starbursting”, and it would therefore lie below our survey limits. Limited attempts to observe fainter galaxies very close to the PG 1211+143 sightline have not yet discovered dwarfs at the absorber redshifts, but we cannot rule out their presence. Indeed, 20 - 30 dwarf galaxies with $L = 0.05 - 0.10L^*$ would be expected at $\sim 15,300 \text{ km s}^{-1}$ given the number of brighter galaxies found in this galaxy group (see Figure 3). If so, the photoionized components could be due to one or more dwarf

superwinds. Colliding dwarf galaxy winds from numerous nearby dwarf galaxies could be responsible for the O VI, since the typical shock velocity would reflect the velocity dispersion in the group ($100 - 200 \text{ km s}^{-1}$). Such a model would also naturally explain the large number of components in the absorption-line systems. PG 1211+143 provides an opportunity to test this model for two absorbers with a deeper galaxy survey in a single field.

4.7. Intragroup medium at $15,300 \text{ km s}^{-1}$?

Even if the O VI at $15,242 \text{ km s}^{-1}$ is not associated with the nearby galaxy, it may still be associated with a hot intragroup medium. As suggested by Mulchaey et al. (1996), spiral-rich groups of galaxies are promising places to look for the predicted warm-hot phase of the IGM. Spiral-rich groups are numerous and may be only marginally bound. By scaling down from elliptical-rich groups with soft X-ray detections, Mulchaey et al. (1996) suggested that if spiral-rich groups possess intragroup gas, they should have physical conditions just right to produce O VI. In this model, spiral-dominated groups are too small and loosely bound to achieve the high temperatures that would make them detectable in the soft X-ray band. Thus, their predicted UV absorption lines would be the best method of direct detection. Spiral-rich groups are numerous, yet they occupy a small volume fraction of the universe. Thus, they represent a potential reservoir for hot baryons that has not been extensively probed by the undirected O VI surveys by *HST* and *FUSE*.

The $15,300 \text{ km s}^{-1}$ absorber toward PG 1211+143 is an excellent candidate for the predicted hot intragroup medium. The PG 1211+143 sightline grazes but does not pierce the spiral-rich group extending $\sim 1 \text{ Mpc}$ away from the sightline to the northwest. Indeed, this O VI absorber exhibits several features predicted by the Mulchaey et al. (1996) model. First, the O VI has column density $N(\text{O VI}) \simeq 10^{14} \text{ cm}^{-2}$, as predicted for a typical group with $T \simeq 10^6 \text{ K}$. The O VI is broad, reflecting both thermal broadening and some contribution from bulk (but perhaps unvirialized) motions in the group. The O VI is too broad to be clearly associated with the C IV or N V, which would instead suggest an origin in photoionized gas. These factors suggest that the $15,300 \text{ km s}^{-1}$ system does arise in a hot intragroup medium. However, there are some significant uncertainties in this picture. First, the O VI linewidth ($b_{\text{OVI}} = 53 \text{ km s}^{-1}$) is narrower than the observed velocity dispersion of the group. However, this may be expected, given that the sightline grazes the edge of the group, rather than piercing the middle. A sightline that follows a chord through a roughly spherical object should show less dispersion than a more central sightline. The second uncertainty with an intragroup origin is that the $19,300 \text{ km s}^{-1}$ system shows two similar O VI components in the absence of a spiral-rich group. Thus, even if the intragroup medium picture suggested by Mulchaey et al. (1996) is accurate, it is clearly not a unique explanation for broad O VI absorption. Nevertheless, we consider the intragroup medium model to be a viable candidate for the origins of collisionally-ionized intergalactic O VI ab-

¹⁰We cannot derive an accurate estimate of the Si/C ratio at $15,300 \text{ km s}^{-1}$ because photoionization models that produce roughly one-to-one column-density ratios $N(\text{C III})/N(\text{C IV})$ and $N(\text{Si III})/N(\text{Si IV})$ imply large and highly uncertain ionization corrections for the unobserved ions C V, Si V, and higher stages. Only a few lines of C and Si are detected at $19,300 \text{ km s}^{-1}$, where the ionization correction is less uncertain and $[\text{Si III/C III}] \simeq [\text{Si/C}] \simeq -0.5$.

sorbers. This model could be tested with better statistics using sightlines that probe groups at different impact parameters, and sightlines known to avoid groups.

If we adopt the hypothesis that the 15,300 km s⁻¹ O VI arises in a hot intragroup medium, we can ask whether this medium has any relation to the photoionized gas in the other components at 15,300 km s⁻¹. In particular, do the lower-ionization components represent partially recombined clumps or filaments that are pressure-confined by the hotter low-density medium? At the peak ionization fraction of O VI ($f_{OVI} = 0.22$ at $\log T = 5.45$), the gas pressure $P/k = 2.24n_H T$ can be calculated from the observed column density of O VI and the line-of-sight extent d :

$$P/k = (1.9 \text{ cm}^{-3} \text{ K}) \left(\frac{N_{OVI}}{10^{14} \text{ cm}^{-2}} \right) \left(\frac{0.1Z_{\odot}}{Z} \right) \left(\frac{1 \text{ Mpc}}{d} \right). \quad (3)$$

We scale to one-tenth solar O abundance and a typical group size of 1 Mpc. For the 15,300 km s⁻¹ O VI absorber, we derive $P/k \simeq 3.8 \text{ cm}^{-3} \text{ K}$ for $\log N(\text{O VI}) = 14.26$ and assuming $d = 900 \text{ kpc}$ and $Z = 0.1Z_{\odot}$. The density implied by this size is $n_H = 6 \times 10^{-6} \text{ cm}^{-3}$ at $\log T = 5.45 \text{ K}$. Roughly one-half solar metallicity is required for this hot gas to be in pressure equilibrium with the PIE component A (the only moderate-ionization component that permits a detailed model), which has 2% metallicity. The factor of five discrepancy in pressure between the two components could be erased by uncertainty in any of the fiducial scaling parameters used in this calculation. However, the component A cloud size of 180 – 400 kpc would be difficult to accommodate within a hot intragroup medium of Mpc scale. The large photoionized component could still be a chance superposition near but outside the group without negative implications for the group model. The other photoionized components are also viable candidates for pressure-confined low-ionization clouds, especially component C, which shows $\gtrsim 40\%$ solar metallicity. However, we lack the necessary constraints on temperature and density to make detailed models. If the other PIE components have similar sizes, either a chance location relative to this group or embedded clumps within the group medium seem unlikely for all of them.

The hot intragroup medium model is viable (Equation 3) if $Z \simeq Z_{\odot}$, $d \sim 1 \text{ Mpc}$, $n_H = 2 \times 10^{-5} \text{ cm}^{-3}$, and there is a 30 – 40 km s⁻¹ nonthermal contribution to the O VI linewidth from bulk motions inside the group. The only factor in our data that casts significant doubt on the intragroup medium model at 15,300 km s⁻¹ is the presence of a similar multi-phase Ly α /O VI absorber at 19,300 km s⁻¹, where there is no evidence of a spiral-dominated group. This qualitative discrepancy is difficult to reconcile with the intragroup medium model for the 15,300 km s⁻¹ system. In fact, the similarity between the 15,300 km s⁻¹ and 19,300 km s⁻¹ O VI absorbers makes it difficult to argue that the nearby group exerts any influence at all on the absorption complex at 15,300 km s⁻¹. Nevertheless, we find the hot intragroup medium to be a viable model until additional evidence is available (although it begs the question of the origin of the metals).

A variant of the intragroup medium model was proposed by Shull, Tumlinson, & Giroux (2003) for the absorber complex at $cz \sim 17,000 \text{ km s}^{-1}$ in the PKS 2155-304 sight-

line. They proposed that the two O VI components arise in warm photoionized gas shocked against the hot intragroup medium filling the group potential. This model is consistent with our findings for the physical conditions in the 15,300 km s⁻¹ system, but it is not unique in light of the 19,300 km s⁻¹ system. If it is accurate, it suggests that O VI may serve as a signpost of the true WHIM, which could be verified by X-ray observations of O VII, O VIII, and other species.

4.8. Metal enrichment by continuous star formation?

We have identified high-metallicity, photoionized material that appears to have a recent connection to nearby galaxies. We also find O VI components with velocity separations that suggest they trace the post-shock regions of a strong shock against the photoionized gas. However, connecting the O VI to the galaxies may extend the chain of inference too far. As discussed in § 4.4 and § 4.6 There is circumstantial evidence that these absorbers are at least associated with the same large-scale structure that formed the nearby galaxies, if not with the galaxies themselves. For a single sightline of $\Delta z = 0.08$, two pairings of IGM absorbers with galaxies at $\rho_{\perp} \lesssim 150h_{70}^{-1} \text{ kpc}$ are extremely unlikely if they are random (even more so in light of the PKS 0405-1219 case, see § 4.2). These absorbers also have stronger Ly α than expected from the Penton et al. (2002) correlation of Ly α equivalent width with ρ_{\perp} . Unfortunately we lack the necessary information (see § 4.6 and Stocke et al. 2004a) to establish firmer grounds for causal relationships. However, if these two systems and the PKS 0405-1219 clouds reside in filaments or intragroup medium and are not associated with unseen satellites, their high level of metal enrichment is surprising.

At least one component in each of the PG 1211+143 absorber complexes exhibits metallicity $Z \gtrsim 0.1Z_{\odot}$, and the highly-ionized O VI has 2 – 6 % solar metallicity. Here we estimate how much continuous star formation it takes to generate 1 – 10% solar metallicity over the relevant range of physical scales. We present two versions of the estimate. First, we scale the estimate to the peak cosmic SFR density from all sources over 1 Gyr. Second, we scale to a Milky Way-like SFR ($\sim 1.0M_{\odot} \text{ yr}^{-1}$) over a 150 kpc region. Both calculations assume a mass yield in metals of $y_m = 0.024 M_{\odot}$ for every M_{\odot} formed into stars, and a baryon density $\Omega_b h^2 = 0.0224$ (Spergel et al. 2003).

First, we estimate the total metal enrichment from all galaxies in time $t = (10^9 \text{ yr}) t_9$, scaled to the peak cosmic SFR density, $\rho(SFR)$. Then the IGM metallicity is given by:

$$\begin{aligned} \frac{Z}{Z_{\odot}} &= \frac{\rho(SFR)y_m t}{\Omega_b h^2 \rho_{cr}(0.02)} \\ &= \frac{(0.1M_{\odot} \text{ yr}^{-1} \text{ Mpc}^{-3})(0.024)(10^9 \text{ yr})t_9}{(0.0224)(1.879 \times 10^{-29} \text{ g cm}^{-3})(0.02)} \\ &= (0.019) \left[\frac{\rho(SFR)}{0.1M_{\odot} \text{ yr}^{-1} \text{ Mpc}^{-3}} \right] t_9 \end{aligned} \quad (4)$$

Thus, $\sim 2\%$ solar metallicity can be achieved in the IGM if star formation proceeds for 1 Gyr at the peak rate of $0.1 M_{\odot} \text{ yr}^{-1} \text{ Mpc}^{-3}$ measured at $z = 1 – 6$ (Steidel et al. 1999; Giavalisco et al. 2004).

We can also estimate the metallicity within a volume of radius 150 kpc, such as that probed by the PG 1211+143 sightline in the halos of the two nearby galaxies. Within a 150 kpc radius, with mean density $\langle n_H \rangle = 10^{-4} \text{ cm}^{-3}$ and mean atomic weight $1.32m_H$, there is $4.6 \times 10^{10} M_\odot$ in gas. A burst of star formation will generate a total mass in metals:

$$\begin{aligned} M_{\text{metals}} &= (1 M_\odot \text{ yr}^{-1}) y_m (10^9 \text{ yr}) t_9 \\ &= (2.4 \times 10^7 M_\odot) t_9 \left[\frac{\text{SFR}}{M_\odot \text{ yr}^{-1}} \right] \end{aligned} \quad (5)$$

Thus, the metallicity is:

$$\begin{aligned} \frac{Z}{Z_\odot} &= \frac{(2.4 \times 10^7 M_\odot) t_9 (\text{SFR}/M_\odot \text{ yr}^{-1})}{(4.6 \times 10^{10} M_\odot) (0.02)} \\ &= (0.026) \left[\frac{\text{SFR}}{M_\odot \text{ yr}^{-1}} \right] t_9 \end{aligned} \quad (6)$$

Thus ~ 1 Gyr is required to achieve 2–3% solar metallicity with steady star formation spread over large volumes. This result suggests that the lower metallicities of the photoionized components may be achieved simply by the gradual buildup of metals from quiescent star formation over 1 Gyr. These absorbers are therefore not necessarily associated with any particular galaxy; they may simply be embedded in large-scale filaments of galaxies, as has been suggested for Ly α clouds and weak metal-line absorbers (Morris et al. 1993; Tripp, Lu & Savage 1998; Impey, Petry & Flint 1999; Penton et al. 2002). Such a model does not naturally explain either the multi-phase nature of these absorbers nor the small line-of-sight sizes for some of them. Steady metal enrichment seems insufficient to explain the higher metallicities we see in component C (40% solar) at 15,300 km s $^{-1}$ and in A (40% solar) and D (90% solar) at 19,300 km s $^{-1}$. Rigby et al. (2002) and Charlton et al. (2002) have emphasized this high metallicity problem in the context of the “weak-Mg II absorbers” found in ground-based spectra at somewhat higher redshifts. These high-metallicity absorbers seem to require a single, metal-enriched unbound galaxy wind, metal-enriched gas tidally stripped from an unseen satellite (see § 4.4), or perhaps, as proposed by Rigby et al. (2002), they are directly associated with unseen stellar populations. Thus the gas metallicities inferred for these multiphase absorption complexes suggest they are related to nearby galaxies.

5. DISCUSSION AND CONCLUSIONS

We have used *HST*/STIS and *FUSE* to study two multi-component, multiphase IGM absorption systems with substantial O VI. These systems have the following important features, for which any viable physical model must account:

1. *They are multiphase:* The observed column densities of O VI in these systems are too high to be consistent with photoionization models based on the lower ions, except for a narrow range of parameter space that implies very large (\sim Mpc) pathlengths together with substantial non-thermal broadening. Although PIE models cannot be excluded conclusively, we believe that most of the O VI arises from collisional

ionization in hot ($T = 100,000 - 300,000$ K) gas. The detection of C III - C IV and Si II - Si IV together with O VI in these absorbers appears to trace multiphase structures composed of hot collisionally-ionized gas and warm photoionized gas possibly located close together or interacting. Dwarf galaxy outflows and, at 15,300 km s $^{-1}$, intragroup medium models are both viable production mechanisms for the hot ionized gas.

2. *They are metal-enriched:* We find that all the metal-line systems here are enriched to at least $\sim 1\%$ solar, and some have $Z/Z_\odot \gtrsim 40\%$. The small metallicity may reflect “pre-enrichment” by early generations of stars, but the higher metallicities suggest recent enrichment by galaxies by way of outflows or tidal stripping.
3. *They lie near galaxies and groups:* The discovery of these two multiphase absorbers in close association with galaxies and their resemblance to high-velocity clouds near the Milky Way (Collins et al. 2004; Fox et al. 2004) provides an important caution, or a critical clue, to the interpretation of O VI absorption in the general IGM. As pointed out by Sembach et al. (2003) for the *FUSE* survey of local O VI, it is unwise to interpret the “IGM” O VI as a single class of absorbers in the absence of detailed galaxy information and/or constraints on lower ionization species.
4. *There is no obvious “unified model”:* The two strong absorption-line systems we study here are quite similar. Both show metal-enriched, multiphase gas, broad O VI, and both lie within $150 h_{70}^{-1}$ kpc of $\sim L^*$ galaxies. However, they also show significant differences. One absorber is associated with a spiral-dominated group, while the other exhibits two strong O VI components.

While we have uncovered two absorbers potentially related to nearby galaxies, there is no statistical evidence that this phenomenon is common. The number of well-studied systems is far too small to allow reliable conclusions about the general nature of O VI-bearing hot gas near galaxies. Intensive searches in the $\lesssim 200 h_{70}^{-1}$ kpc regions around galaxies and nearby QSO absorbers should be undertaken to determine the extent to which our results and those of Sembach et al. (2003) can be generally applied to theories of galaxy formation and evolution. The dwarf-galaxy outflow model can be tested by deeper galaxy surveys in this field, but the intragroup medium model will require more high-quality data on QSO sightlines passing through known galaxy groups.

As discussed by Tripp et al. (2001) for an O VI absorber of similar strength in the sightline to H1821+643, the X-ray lines of O VII and O VIII might distinguish the true nature of the hot gas we detect here, if present or future X-ray spectrographs can achieve limiting column densities of $\log N(\text{O VII}) \simeq 14$. Such a test could eliminate the remaining PIE scenarios for the O VI absorbers and better constrain their temperatures. However, at the present time, sensitivity to column densities as low as $\log N(\text{O VII}) = 15$ is available only in rare cases, such as when blazars

flare (Mrk 421; Nicastro et al. 2004). The study by Fang et al. (2002) using Chandra's LETG show that this column density sensitivity will be difficult if not impossible to achieve on a consistent basis in the near term, and may require Constellation-X or later generation instruments.

We thank Brian Keeney for his help with the galaxy survey work and Todd Tripp for comments that improved the manuscript. This work is based on data obtained for the Guaranteed Time Team by the NASA-CNES-CSA *FUSE* mission operated by the Johns Hopkins University. Financial support to U.S. *FUSE* participants has been provided by NASA contract NAS5-32985. J. M. S. and M. L. G. acknowledge the support of NASA LTSA grant NAG5-7262 and NSF grant AST02-06042. J. T. S. and J. M. S. ac-

knowledge support from HST GO-8571.01-A, GO-8192.01-A, GO-6593.01-A, and AR-9221.01-A grants for various studies of the low- z Ly α forest. J. T. acknowledges support by the Department of Astronomy and Astrophysics at the University of Chicago and HST GO-9874.01-A. Based on observations made with the NASA/ESA Hubble Space Telescope, obtained at the Space Telescope Science Institute, which is operated by the Association of Universities for Research in Astronomy, Inc., under NASA contract NAS 5-26555. Ground-based data were obtained with the Apache Point Observatory 3.5-meter telescope, which is owned and operated by the Astrophysical Research Consortium. We have made extensive use of the NED, SIMBAD, and ADS online databases.

REFERENCES

Allende Prieto, C., et al. 2001a, ApJ, 556, L63
 Allende Prieto, C., et al. 2001b, ApJS, 573, 137
 Bahcall, J. N., et al. 1993, ApJS, 87, 1
 Bowen, D. V., Pettini, M., & Blades, J. C. 2002, ApJ, 580, 169
 Bowen, D. V., Tripp, T. M., & Jenkins, E. B. 2001, ApJ, 121, 1456
 Cen, R., & Ostriker, J. P. 1999, ApJ, 519, L109
 Charlton, J. C., Churchill, C. W., Ding, J., Zonak, S., Bond, N., & Rigby, J. R. 2002, in *Extragalactic Gas at Low Redshift*, ed. J. Mulchaey & J. Stocke (Provo: ASP), 122
 Chen, H.-W., & Prochaska, J. X. 2000, ApJ, 543, L9
 Chen, H.-W., Lanzetta, K. M., Webb, J. K., & Barcons, X. 2001, ApJ, 559, 654
 Collins, J. A., Shull, J. M., & Giroux, M. L. 2004, ApJ, 605, 216
 Danforth, C. W., & Shull, J. M. 2004, in "Astrophysics in the Far Ultraviolet: Five Years with *FUSE*", astro-ph/0408262
 Davé, R., et al. 1999, ApJ, 552, 473
 Davé, R., & Tripp, T. M. 2001, ApJ, 553, 528
 Draine, B. T., & McKee, C. F. 1993, ARA&A, 31, 373
 Fang, T., Marshall, H. L., Lee, J. C., Davis, D. S., & Canizares, C. R. 2002, ApJ, 572, L127
 Ferland, G. J., et al. 1998, PASP, 110, 761
 Fox, A. J., et al. 2004, ApJ, 602, 738
 Fukugita, M., Hogan, C. J., & Peebles, P. J. E. 1998, ApJ, 503, 518
 Giavalisco, M., et al. 2004, ApJ, 600, L103
 Huchra, J., Geller, M., Clemens, C., Tokarz, S., & Michel, A. 1992, Bulletin C. D. S. 41, 31
 Impey, C. D., Petry, C. E., & Flint, K. P. 1999, ApJ, 524, 536
 Indebetouw, R., & Shull, J. M. 2004a, ApJ, 605, 205
 Indebetouw, R., & Shull, J. M. 2004b, ApJ, 607, 309
 Keeney, B. A., Momjian, E., Stocke, J. T., Carilli, C. L., & Tumlinson, J. 2005, ApJ, submitted (astro-ph/0409448)
 Lanzetta, K. M., Bowen, D. V., Tytler, D., & Webb, J. K. 1995, ApJ, 442, 538
 Marzke, R. O., Huchra, J. P., & Geller, M. J. 1994, ApJ, 428, 43
 McLin, K. M. 2002, Ph. D. Thesis, University of Colorado
 Moos, H. W., et al. 2000, ApJ, 538, L1
 Morris, S. L., et al. 1993, ApJ, 419, 524
 Mulchaey, J. S., Mushotzky, R. F., Burstein, D., & Davis, D. S. 1996, ApJ, 456, L5
 Nicastro, F., Zezas, A., Drake, J., Elvis, M., Fiore, F., Fruscione, A., Marengo, M., Mathur, S., & Bianchi, S. 2002, ApJ, 573, 157
 Nicastro, F., et al. 2004, ApJ, submitted
 Penton, S. V., Shull, J. M., & Stocke, J. T. 2000, ApJ, 544, 150
 Penton, S. V., Stocke, J. T., & Shull, J. M. 2002, ApJ, 565, 720
 Penton, S. V., Stocke, J. T., & Shull, J. M. 2004, ApJS, 152, 29
 Prochaska, J. X., Chen, H.-W., Howk, J. C., Weiner, B. J., & Mulchaey, J. 2004, ApJ, in press (astro-ph/0408294)
 Rigby, J. R., Charlton, J. C., & Churchill, C. W. 2002, ApJ, 565, 743
 Rosenberg, J. L., Ganguly, R., Giroux, M. L., & Stocke, J. T. 2003, ApJ, 591, 677
 Sahnou, D. J., et al. 2000, ApJ, 538, L7
 Savage, B. D., & Sembach, K. R. 1991, ApJ, 379, 245
 Savage, B. D., Sembach, K. R., Tripp, T. M., & Richter, P. R. 2002, ApJ, 564, 631
 Sembach, K. R., Howk, J. C., Savage, B. D., Shull, J. M., & Oegerle, W. R. 2001, ApJ, 561, 573
 Sembach, K. R., et al. 2003, ApJS, 146, 165
 Sembach, K. R. 2003 Proc. STScI Symposium "The Local Group as an Astrophysical Laboratory", astro-ph/0311089
 Shapiro, P. R., & Moore, R. T. 1976, ApJ, 207, 460
 Shull, J. M., & McKee, C. F. 1979, ApJ, 227, 131
 Shull, J. M., Roberts, D., Giroux, M. L., Penton, S. V., & Fardal, M. A. 1999, AJ, 118, 1450
 Shull, J. M., Tumlinson, J., & Giroux, M. L. 2003, ApJ, 594, L107
 Spergel, D. N., et al. 2003, ApJ, 148, 175
 Steidel, C. C. 1995, in *QSO Absorption Lines*, ed. G. Meylan (Garching: Springer), 139
 Steidel, C. C. 1998, in *Galaxy Halos*, ed. D. Zaritsky (Provo: ASP), 167
 Steidel, C. C., Adelberger, K. L., Giavalisco, M., Dickenson, M., & Pettini, M. 1999, ApJ, 519, 1
 Stocke, J. T., Keeney, B. A., McLin, K. M., Rosenberg, J. L., Weymann, R. J., & Giroux, M. L. 2004a, ApJ, 609, 94
 Stocke, J. T., Shull, J. M., & Penton, S. V. 2004b, Proc. STScI Symposium "Planets to Cosmology", astro-ph/0407352
 Sutherland, R. S., & Dopita, M. A. 1993, ApJS, 88, 253
 Tripp, T. M., Lu, L., & Savage, B. D. 1998, ApJ, 508, 200
 Tripp, T. M., Savage, B. D., & Jenkins, E. B. 2000, ApJ, 534, L1
 Tripp, T. M., Giroux, M. L., Stocke, J. T., Tumlinson, J., & Oegerle, W. R. 2001, ApJ, 563, 724
 Tripp, T. M., et al. 2002, ApJ, 575, 697
 Tumlinson, J., Giroux, M. L., Shull, J. M., & Stocke, J. T. 1999, AJ, 118, 2148
 van Gorkom, J. H., Bahcall, J. N., Jannuzzi, B. T., & Schneider, D. P. 1993, AJ, 106, 2213

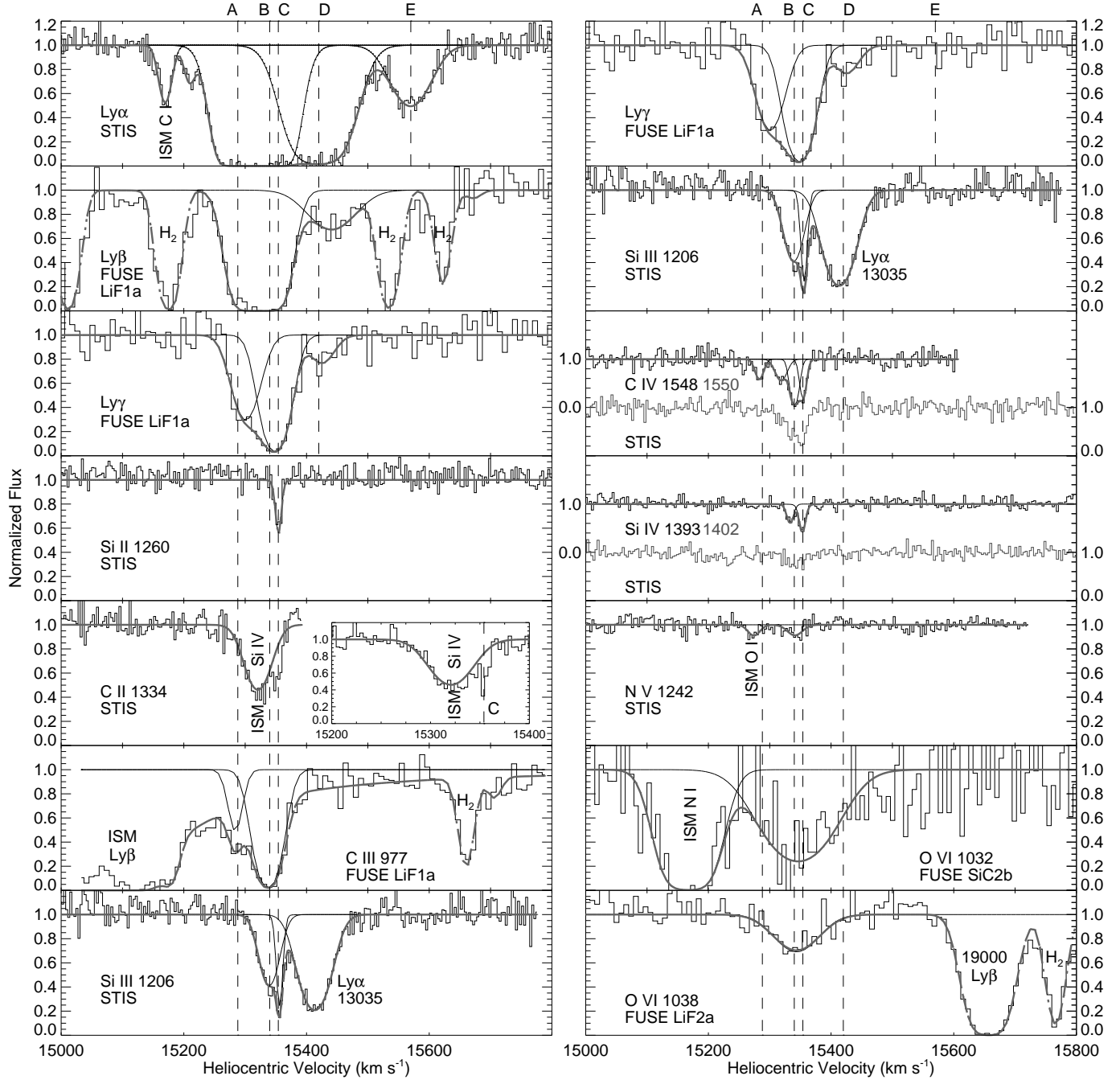


FIG. 1.— The absorption lines in the $15,300 \text{ km s}^{-1}$ system, aligned in heliocentric velocity space. The panels are marked with the species of interest and the source of the data (*FUSE* or *STIS*). The components from Table 2 are marked in vertical dashed lines, and labeled at the top. Black profiles are the individual model components, and thick gray lines trace the overall model line profiles. Contaminating Galactic absorption is labeled (H_2 , $\text{Ly}\beta$, C I , N I , O I , Si IV , including model fits where necessary). The panel with $\text{C II } \lambda 1334$ shows the same line on two adjacent *STIS* echelle orders, where Component C in $\text{C II } \lambda 1334$ lies in the wing of Galactic $\text{Si IV } \lambda 1402$. In both cases, the plotted model was derived from a fit to the Galactic $\text{Si IV } \lambda 1393$ line and then applied directly to the $\lambda 1402$ profile to show the excess absorption by C II at $15,353 \text{ km s}^{-1}$. In the right column, $\text{H I } \text{Ly}\gamma$ and $\text{Si III } \lambda 1206$ are repeated to ease visual comparisons of the high-ion components with the lower ions and H I . The $\text{N V } \lambda 1238$ line is not shown because it lies directly underneath the strong Galactic ISM $\text{O I } \lambda 1302$ line. For C IV and Si IV , we plot both lines of the doublet; the stronger line is plotted above and corresponds to the left side axis, while the weaker and bottom line corresponds to the right hand axis.

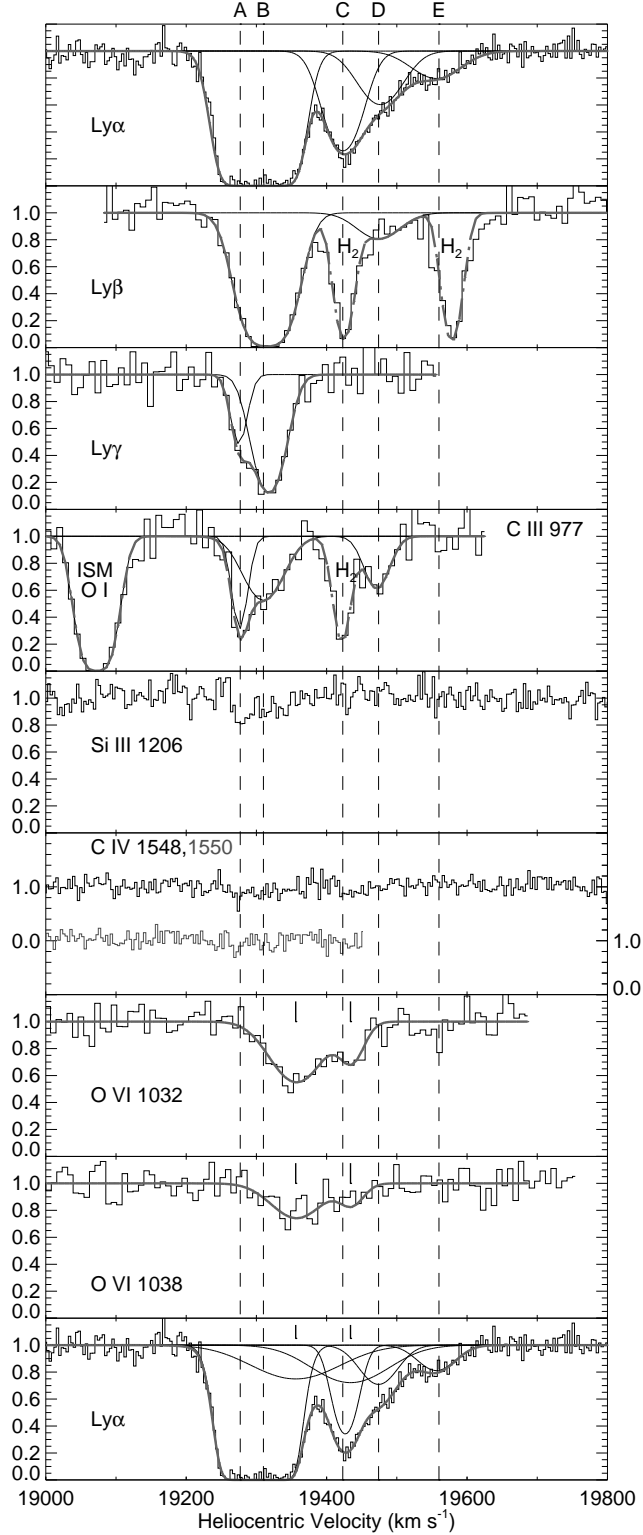


FIG. 2.— The absorption lines in the $19,300 \text{ km s}^{-1}$ system, aligned in heliocentric velocity space. The components from Table 3 are marked in vertical dashed lines, and labeled at the top. Black profiles are the individual model components, and thick gray lines trace the combined model profiles. Contaminating Galactic absorption is labeled where it exists (O I, H₂). Si III $\lambda 1206$ does not show a model fit because its column density was obtained by direct integration of the data. For C IV we plot data covering both lines of the undetected doublet; the stronger line is plotted above and corresponds to the left side axis, while the weaker and bottom line corresponds to the right hand axis. The bottom panel shows a model incorporating possible H I associated with collisionally ionized O VI components into the Ly α profile. The two additional components are included here and the line centroids of these two components are marked with ticks in the lower three panels (see § 3.2).

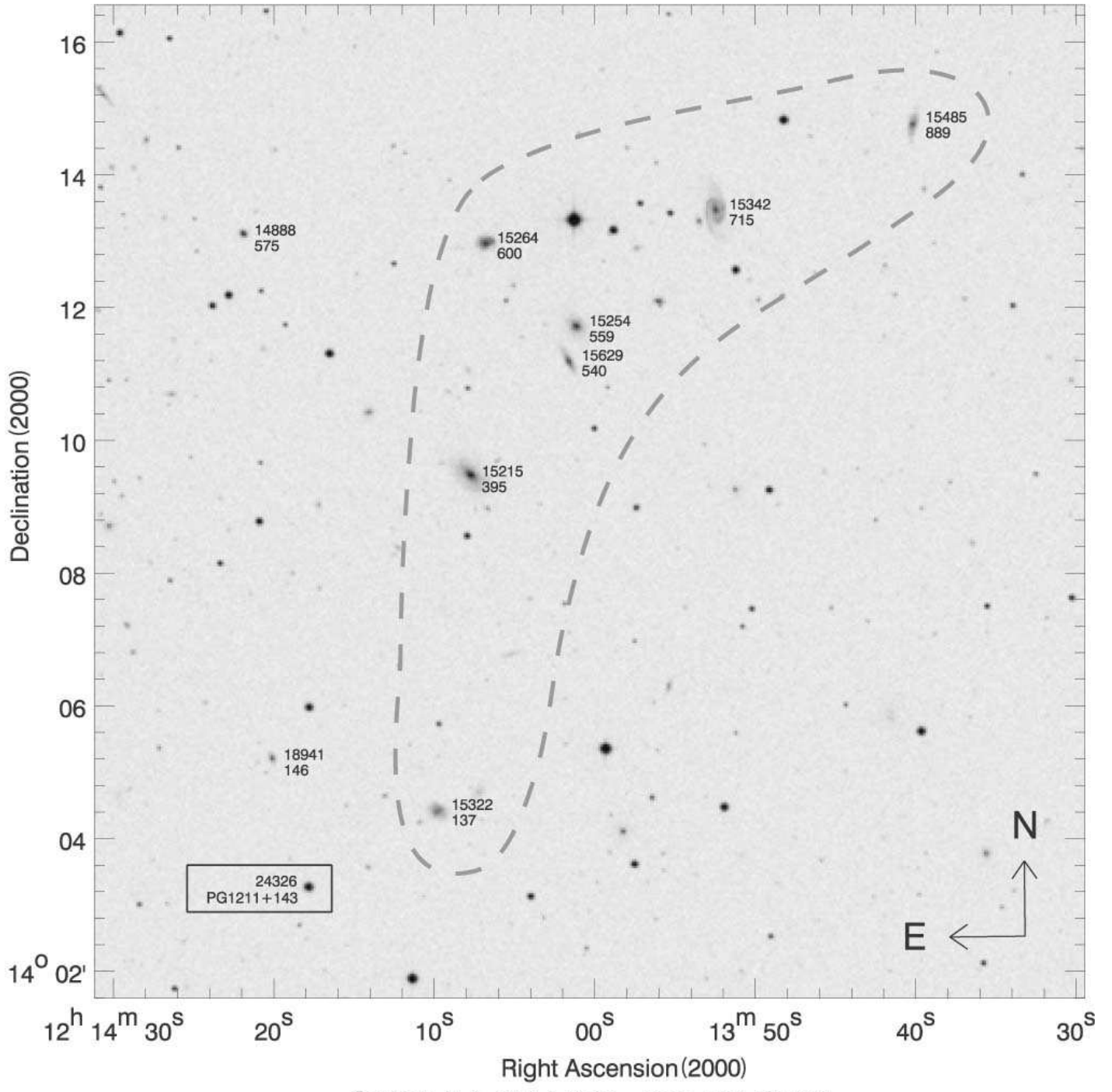


FIG. 3.— The sky around PG 1211+143. This $15' \times 15'$ image from the POSS2 blue plates was obtained online from STScI. PG 1211+143 lies at lower left. The galaxy group associated with the $15,300 \text{ km s}^{-1}$ absorber complex extends to the northwest as marked. The isolated galaxy associated with the $19,300 \text{ km s}^{-1}$ absorbers lies $\sim 2'$ north of the QSO. The galaxies are labeled with their heliocentric velocity (cz_{gal} in km s^{-1}) and their projected distance ($h_{70}^{-1} \text{ kpc}$) to the QSO sightline at cz_{gal} . These distances assume a flat universe with $H_0 = 70 \text{ km s}^{-1} \text{ Mpc}^{-1}$, $\Omega_m = 0.3$, and $\Omega_\Lambda = 0.7$. In an attempt to determine whether the $15,300 \text{ km s}^{-1}$ galaxy group and/or filament extends SE beyond PG 1211+143, the galaxy field was surveyed $3 - 5'$ to the S and E of the QSO. We obtained 8 redshifts in the quadrants S and E of the displayed field and made no additional discoveries of galaxies at the same redshifts as the absorbers.

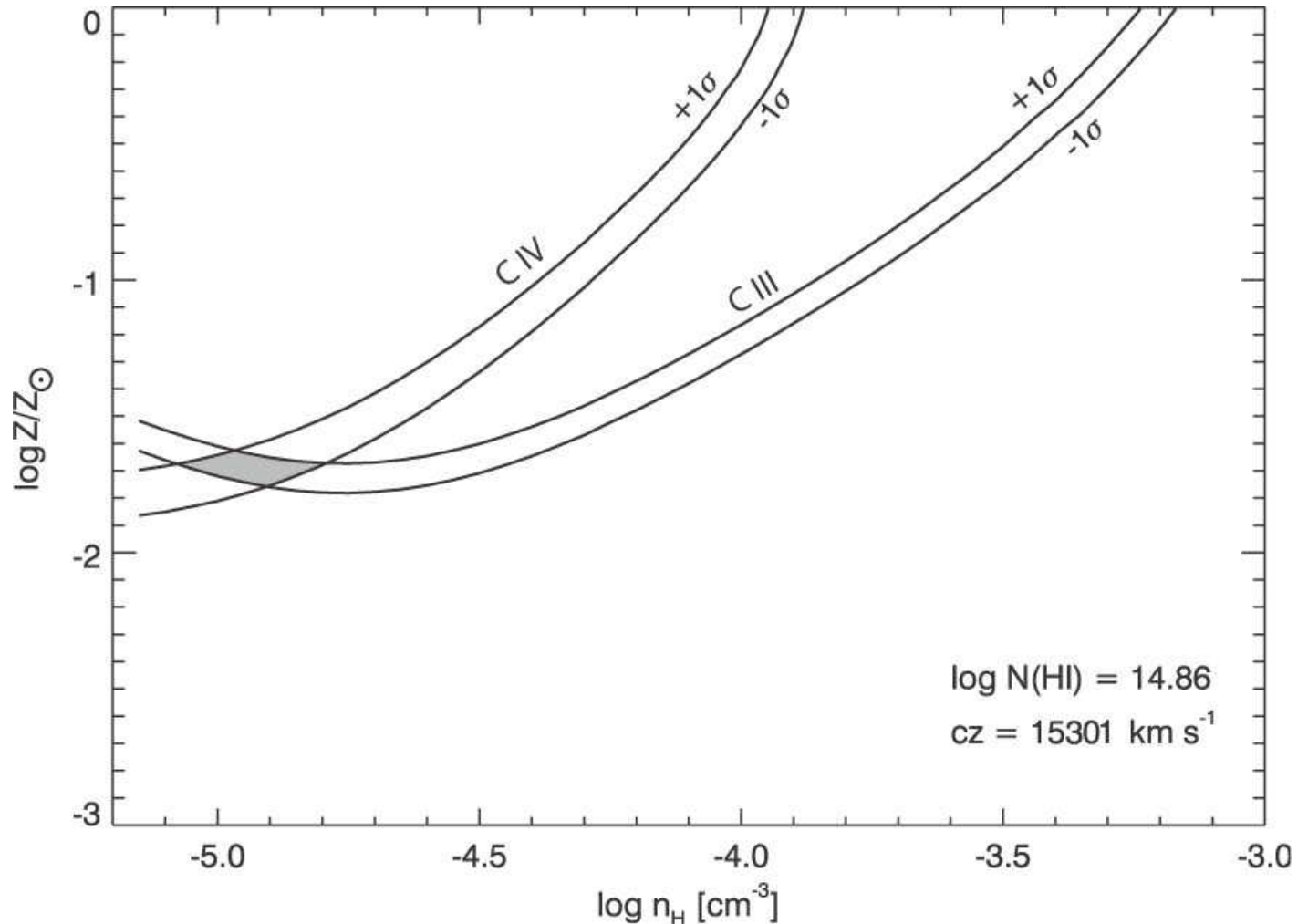


FIG. 4.— The density-metallicity parameter space for the A component ($15,301 \text{ km s}^{-1}$) of the $15,300 \text{ km s}^{-1}$ system. The permitted range of parameters is marked with the shaded region, where the $\pm 1\sigma$ ranges of permitted column density for C III and C IV overlap.

TABLE 1
GALAXIES IN THE PG 1211+143 FIELD

RA (J2000)	DEC (J2000)	m_B^a (Source)	cz^b (km s $^{-1}$)	ρ_{\perp}^c (h_{70}^{-1} kpc)	Redshift Source
12:14:19.9	14:05:10	17.9(3)	18,941	146	Stocke
12:14:21.4	14:13:04	18.0(3)	14,888	575	Stocke
12:13:39.5	14:14:40	17.7(2)	15,485	889	CfA
12:13:51.8	14:13:23	15.7(1)	15,342	715	CfA
12:14:00.6	14:11:39	17.5(2)	15,254	559	CfA
12:14:01.1	14:11:08	18.0(2)	15,629	540	CfA
12:14:06.3	14:12:55	16.8(2)	15,264	600	CfA
12:14:07.4	14:09:24	15.3(1)	15,215	395	CfA
12:14:09.5	14:04:23	17.3(3)	15,322	137	CfA
12:14:17.7	14:03:14	14.6(1)	24,326	0	PG 1211+143

^aB band apparent magnitude taken from (1) CfA, (2) NED (<http://nedwww.ipac.caltech.edu>), or (3) Stocke et al. (2005, in preparation).

^bHeliocentric velocity.

^cProjected galaxy/sightline separations at the individual galaxy redshifts. These distances assume a flat universe with $H_0 = 70$ km s $^{-1}$ Mpc $^{-1}$, $\Omega_M = 0.3$, and $\Omega_\Lambda = 0.7$.

TABLE 2
THE 15,300 KM s⁻¹ SYSTEM

Ion/Line	<i>cz</i> (km s ⁻¹) ^a	$\log N$ (cm ⁻²)	<i>b</i> (km s ⁻¹)	Group	$N(v)$ ^b
H I Ly α	15,315 $^{+8}_{-19}$	15.21 $^{+0.60}_{-0.50}$	36 $^{+3}_{-7}$	A-C*	saturated
	15,407 $^{+20}_{-7}$	14.57 $^{+0.05}_{-0.27}$	49 $^{+4}_{-9}$	D	...
	15,570 $^{+3}_{-3}$	13.54 $^{+0.05}_{-0.05}$	37 $^{+3}_{-4}$	E	...
H I Ly β	15,323 $^{+10}_{-10}$	15.60 $^{+0.30}_{-0.10}$	32 $^{+2}_{-5}$	A-C*	saturated
	15,435 $^{+10}_{-10}$	14.20 $^{+0.06}_{-0.06}$	45 $^{+10}_{-10}$	D	...
H I Ly γ	15,301 $^{+10}_{-10}$	14.86 $^{+0.10}_{-0.10}$	22 ^c	A	15.43 ± 0.08
	15,349 $^{+10}_{-10}$	15.31 $^{+0.05}_{-0.05}$	21 $^{+2}_{-2}$	B-C*	...
	15,425 $^{+10}_{-10}$	14.10 $^{+0.65}_{-0.15}$	14 $^{+10}_{-13}$	D	...
C II 1334	15,353 $^{+3}_{-3}$	13.15 $^{+0.10}_{-0.09}$	6 $^{+2}_{-2}$	C	blend
C III 977	15,284 $^{+10}_{-10}$	12.99 $^{+0.05}_{-0.05}$	8 ^d	A	13.86 ± 0.15
	15,337 $^{+10}_{-10}$	13.92 $^{+0.11}_{-0.04}$	20 $^{+2}_{-3}$	B	...
	15,354 ^e	14.14 ^f	4	C/C*	...
C IV 1548	15,283 $^{+3}_{-3}$	13.02 $^{+0.08}_{-0.08}$	8 $^{+4}_{-2}$	A	14.03 ± 0.06
	15,319 $^{+3}_{-3}$	13.08 $^{+0.13}_{-0.12}$	9 $^{+5}_{-2}$
	15,340 $^{+3}_{-3}$	13.75 $^{+1.00}_{-0.17}$	6 $^{+3}_{-4}$	B*	...
	15,354 $^{+3}_{-3}$	13.43 $^{+0.16}_{-0.27}$	5 $^{+2}_{-3}$	C*	...
Si II 1260	15,354 $^{+3}_{-3}$	12.25 $^{+0.05}_{-0.05}$	5 $^{+1}_{-1}$	C	12.29 ± 0.12
Si III 1206	15,342 $^{+3}_{-3}$	12.82 $^{+0.05}_{-0.06}$	20 $^{+2}_{-2}$	B	12.99 ± 0.05
	15,356 $^{+3}_{-3}$	12.37 $^{+0.10}_{-0.10}$	5 ^g	C*	...
Si IV 1393	15,334 $^{+3}_{-3}$	12.49 $^{+0.08}_{-0.05}$	7 $^{+1}_{-1}$	B*	12.96 ± 0.05
	15,353 $^{+3}_{-3}$	12.67 $^{+0.05}_{-0.07}$	5 $^{+2}_{-1}$	C*	...
N V 1242	15,341 $^{+4}_{-5}$	12.98 $^{+0.13}_{-0.20}$	15 $^{+8}_{-8}$	B*	...
O VI 1038	15,341 $^{+10}_{-10}$	14.26 $^{+0.05}_{-0.08}$	53 $^{+10}_{-9}$...	14.21 ± 0.08

^aErrors in velocity are constrained to \geq one-half the resolution element; ± 10 km s⁻¹ for *FUSE*, ± 3 km s⁻¹ for STIS/E140M.

^bColumn density calculated from apparent optical depth integration of the observed profiles over $v = 15,250$ -15,450 km s⁻¹.

^cThis component was forced to have $b = 22$ km s⁻¹ (H I at $T \simeq 30,000$ K). If all parameters are allowed to float, we obtain $\log N(\text{H I}) = 14.77$, $b = 6$ km s⁻¹ for component A, and $\log N(\text{H I}) = 15.38$ and $b = 26$ km s⁻¹ for components B - C*. The listed parameters are adopted in the models in § 3.

^dThis C III fit is poorly constrained. The tabulated N and cz were fitted with a fixed $b = 8$ km s⁻¹ from the C IV component A.

^eThis velocity was fixed at Si II component C.

^fThe addition of this narrow C III fixed at 15,354 km s⁻¹ does not change the fits for A and B by more than their assigned errors, but it carries uncertainty of ~ 1.0 dex in $N(\text{C III})$. The listed parameters for A and B do not include C; for C they are the overall best fit with cz fixed at 15,354 km s⁻¹.

^gThis component fitted with $b = 5$ km s⁻¹ fixed from Si IV component C*.

TABLE 3
THE 19,300 KM S⁻¹ SYSTEM

Ion/Line	<i>cz</i> (km s ⁻¹) ^a	$\log N(\text{cm}^{-2})$	<i>b</i> (km s ⁻¹)	Group	<i>N(v)</i> ^b
H I Ly α	19,305 $^{+3}_{-3}$	14.94 $^{+0.07}_{-0.05}$	34 $^{+2}_{-2}$	A+B	saturated
	19,423 $^{+3}_{-3}$	13.69 $^{+0.05}_{-0.06}$	27 $^{+2}_{-2}$	C	...
	19,474 ^c	13.40 $^{+0.16}_{-0.22}$	35 $^{+11}_{-11}$	D	...
	19,560 $^{+4}_{-5}$	12.87 $^{+0.08}_{-0.10}$	28 $^{+6}_{-5}$	E	...
H I Ly β	19,315 $^{+10}_{-10}$	15.12 $^{+0.06}_{-0.05}$	30 $^{+2}_{-3}$	A+B	saturated
	19,474 ^d	13.65 $^{+0.15}_{-0.30}$	35 ^d	D	...
H I Ly γ	19,278 $^{+10}_{-10}$	14.46 $^{+0.12}_{-0.05}$	11 $^{+2}_{-1}$ ^e	A	15.18 ± 0.06
	19,317 $^{+10}_{-10}$	15.09 $^{+0.06}_{-0.07}$	21 $^{+3}_{-3}$	B	...
C III 977	19,277 $^{+10}_{-10}$	13.89 $^{+1.10}_{-0.70}$	4 $^{+5}_{-2}$ ^f	A	13.50 ± 0.08
	19,310 $^{+10}_{-10}$	13.23 $^{+0.10}_{-0.06}$	27 $^{+9}_{-6}$	B	...
	19,474 $^{+10}_{-10}$	12.96 $^{+0.05}_{-0.04}$	18 $^{+6}_{-9}$	D	13.02 ± 0.08
C IV 1548	...	$\leq 12.5^g$	< 13.1 ^h
Si II 1260	...	$\leq 11.5^g$
Si III 1206	...	12.20 $^{+0.08}_{-0.08}$...	A	...
Si IV 1393	...	$\leq 12.0^g$	< 12.6 ^h
N V 1242	...	$\leq 12.2^g$	< 12.8 ^h
O VI 1032	19,356 $^{+10}_{-10}$	14.08 $^{+0.05}_{-0.06}$	37 $^{+7}_{-6}$...	14.04 ± 0.08
	19,434 $^{+10}_{-10}$	13.63 $^{+0.11}_{-0.20}$	21 $^{+10}_{-10}$	C?	13.75 ± 0.05

^aErrors in velocity are constrained to \geq one-half the resolution element; ± 10 km s⁻¹ for FUSE, ± 3 km s⁻¹ for STIS/E140M.

^bColumn density calculated from apparent optical depth integration of the observed profiles over $v = 19,300\text{--}19,490$ km s⁻¹. For O VI the integrals range over $v = 19,300\text{--}19,390$ km s⁻¹ and $v = 19,390\text{--}19,490$ km s⁻¹. For limits on C IV, Si IV, and N V, see note *h*.

^cVelocity poorly constrained; fixed at position of C III D component.

^dFor this component, the *N* was fitted with *cz* fixed at the velocity of C III D component and *b* fixed at the value from the Ly α D component.

^eThe *b*-value for this component was limited to $b > 10$ km s⁻¹ to accommodate the presence of C III in photoionized gas at $T > 8000$ K.

^fThis formal best-fit linewidth is strictly too narrow for FUSE to resolve. The formal error bar on *N*(C III) is large enough to overlap the value provided by direct integration. Implications for the absorber model are discussed in § 3.2.

^g4 σ upper limits, signal-to-noise determined in 2-pixel resolution elements ($R = 44,000$).

^h4 σ upper limits, integrated over 100 km s⁻¹ velocity range for comparison to detected O VI lines in CIE. See Section 3.2 for details.

TABLE 4
METALLICITIES FOR THE DETECTED COMPONENTS

Label	v (km s $^{-1}$)	Z/Z_{\odot}
15,300 km s $^{-1}$		
A	15,288	0.02 ± 0.005
B-C*	15,340-15,354	$\gtrsim 0.40^a$
19,300 km s $^{-1}$		
A	19,274	≥ 0.4
B	19,317	$0.05 - 0.25$
D	19,474	≥ 0.6
O VI	19,356	≥ 0.06
O VI	19,434	≥ 0.02

^aEstimate for blended components B,B*, C, and C* derived from photoionization considerations. See § 3.1 for discussion.

TABLE 5
SHOCK MODELS FOR 19,300 KM S $^{-1}$ O VI

Label	Δv^a (km s $^{-1}$)	$\log T_s$ (K)	b_{th} (km s $^{-1}$)	c_s^b (km s $^{-1}$)	Mach number
19,356 km s $^{-1}$					
A	+137	5.41	16	14-20	7-10
B	+68	4.79
C	-116	5.27
D	-204	5.76	24	18-22	9-11
E	-353	6.24	42	~ 33	~ 11
19,434 km s $^{-1}$					
A	+272	6.00	32	14-20	14-19
B	+202	5.75	24	14-30	7-14
C	+19	3.70
D	-69	4.82
E	+218	5.82	26	~ 33	~ 7

^aScaled up by $\sqrt{3}$ to account for average 3D to 1D projection effects.

^bAdiabatic sound speed $c_s \equiv (\gamma kT/\mu)^{1/2}$ with $\mu = 0.6m_H$ and $\gamma = 5/3$.

TABLE 6
COMPARISONS TO GALACTIC O VI HVCs

System	$\log \left(\frac{\text{Si IV}}{\text{O VI}} \right)$	$\log \left(\frac{\text{C IV}}{\text{O VI}} \right)$	$\log \left(\frac{\text{N V}}{\text{O VI}} \right)$	Note
PKS 2155-304	-1.02 ± 0.08	-0.32 ± 0.06	< -0.72	1
PKS 2155-304	-1.30 ± 0.16	0 ± 0.06	< -0.47	2
Mrk 509	< -1.36	-0.36 ± 0.06	< -0.81	3
Mrk 509	-0.4 ± 0.2	0.22 ± 0.02	< -0.69	4
PG 1259+593	-1.0 ± 0.1	0.46 ± 0.06	< 1.15	5
PG 1211+143	-1.25 ± 0.07	-0.18 ± 0.07	-1.23 ± 0.12	6
PG 1211+143	< -1.4	< -0.9	< -1.2	7
PG 1211+143	< -1.2	< -0.7	< -1.0	8

NOTE.—(1) Component 1 ($V_{LSR} = -140 \text{ km s}^{-1}$) toward PKS 2155-304 (2) Component 2 ($V_{LSR} = -270 \text{ km s}^{-1}$) toward PKS 2155-304 (3) Component 1 ($V_{LSR} = -240 \text{ km s}^{-1}$) toward Mrk 509 (4) Component 2 ($V_{LSR} = -300 \text{ km s}^{-1}$) toward Mrk 509. The PKS 2155-304 and Mrk 509 data are from Collins, Shull, & Giroux 2004. (5) Fox et al. 2004 (6) integrated column density over $v = 15,250 - 15,450 \text{ km s}^{-1}$ (7) integrated column density over $v = 19,300 - 19,390 \text{ km s}^{-1}$ (8) integrated column density over $v = 19,390 - 19,490 \text{ km s}^{-1}$.